CROSSLINK-DEPENDENT PULMONARY TOXICITY OF PNIPAM-AAC MICROGEL AGGREGATES

A Dissertation
Presented to
The Academic Faculty

by

John Michael Nicosia

In Partial Fulfillment
of the Requirements for the Degree
Doctor of Philosophy in the
Wallace H. Coulter Department of Biomedical Engineering

Georgia Institute of Technology
Emory University
May, 2019

CROSSLINK-DEPENDENT PULMONARY TOXICITY OF PNIPAM-AAC MICROGEL AGGREGATES

Approved by:

Dr. Thomas H. Barker, Co-Advisor
School of Biomedical Engineering
University of Virginia

Dr. Wilbur A. Lam, Co-Advisor
School of Biomedical Engineering
Georgia Institute of Technology

Dr. Philip J. Santangelo
School of Biomedical Engineering
Georgia Institute of Technology

Dr. Gabriel A. Kwong
School of Biomedical Engineering
Georgia Institute of Technology

Dr. Alberto Fernández-Nieves
School of Physics
Georgia Institute of Technology

Dr. Ashley C. Brown
School of Biomedical Engineering
North Carolina State University

Date Approved: March 6th, 2019

I dedicate this thesis to my father, Peter Nicosia, who sparked my scientific curiosity when I was a child, and never grew tired of my incessant questions.

ACKNOWLEDGEMENTS

If it takes a village to raise a child, it must at least take a neighborhood of exhausted academics to graduate a PhD student. To begin, I want to thank my advisor, Dr. Thomas Barker, for his sustained support and flexibility throughout my degree. Between changing my project halfway through, choosing to remain in Atlanta when he moved his lab to Virginia, and then changing my project one more time near the end of my PhD, I certainly have not been the easiest student to advise. But throughout it all, Tom continually allowed me to define my own path and was supportive of all the research and professional development activities I pursued. Along the same lines, I want to thank Dr. Wilbur Lam, for graciously agreeing to co-advise me so that I could remain in Atlanta after Tom left.

I could not have finished this work without the technical advice and assistance of a host of talented people, especially Dwight Chambers, Jonas Cuadrado, Meredith Fay, Yumiko Sakurai, Dan Abebayehu, Sue Landes, and Mary Harp. For our long hours staring at AFM probes and digesting soft matter physics together, Dwight deserves a specific shout-out. Similarly, I am grateful for the expert input of my committee members Alberto Fernández-Nieves, Phil Santangelo, Gabe Kwong, and especially Ashley Brown, without whom this project would never have existed.

The members of both the Barker and Lam labs have made my life in graduate school much more pleasant, and I want to thank Dwight Chambers, Haylee Bachman, Riley Hannan, Leandro Moretti, and Meredith Fay in particular.

Finally, I must thank my family and friends, for putting up with me throughout this long process. Beyond anything, I am truly grateful for my fiancée, Natalie Mitchell, who has somehow remained by my side this whole time. Without her endless support and encouragement during some of the most difficult times of my life, I am confident I would not have been able to finish this degree.

TABLE OF CONTENTS

LIST OF TABLES

LIST OF FIGURES

LIST OF SYMBOLS AND ABBREVIATIONS

AAc	Acrylic Acid
AFM	Atomic Force Microscopy
ApoB100	Apolipoprotein B-100
APS	Ammonium Persulfate
BALF	Bronchoalveolar Lavage Fluid
BIS	N,N'-methylenebisacrylamide
cCHP	Cationic Cholesterol-bearing Pullulan
DLS	Dynamic Light Scattering
DOTA	1,4,7,10-tetraazacyclododecane-1,4,7,10-tetraacetic acid
dPG	Dendritic Polyglycerol
H&E	Hemotoxylin and Eosin
ICG	Indocyanine Green
IgG	Immunoglobulin G
IHC	Immunohistochemistry
LCST	Lower Critical Solution Temperature
MPS	Mononuclear Phagocytic System
MRI	Magnetic Resonance Imaging
MS	Mass Spectrometry
MSB	Martius Scarlet Blue
NIR	Near-infrared
NIR-CHP	IRDye800-loaded Cholesterol-modified Pullulan
ODN	Antisense Oligodeoxynucleotides

PBAE	Poly(β-amino ester)
PBS	Phosphate-buffered Saline
PEG	Polyethylene Glycol
PEI	Polyethylenimine
PET	Positron emission tomography
PLP	Platelet-like Particle
PMA	Poly(methyl acrylate)
pNIPAM	Poly(N-isopropylacrylamide)
pNIPAM-AAc	Poly(N-isopropylacrylamide)-co-acrylic acid
pNIPMAM	poly(N-isopropylmethacrylamide)
RBC	Red Blood Cell
sdFv	Single Domain Antibody Fragment
SLN	Sentinal Lymph Node
ULC	Ultra-low crosslinked
VPTT	Volume Phase Transition Temperature

SUMMARY

Microgels, also referred to as nanogels, are hydrophilic polymer networks synthesized into micro- or nano-sized hydrogel particles. Due to their relative ease of synthesis and highly tunable properties, they have been explored extensively for a range of biomedical applications, including therapeutic delivery, imaging, and biosensors. Yet despite decades of research, only a handful of microgel-based technologies have reached clinical trials. Primary barriers to clinical translation of microgels include rapid clearance from circulation and toxicity or off-target effects. While there have been many advancements in microgel research, there still exists a lack of understanding of the factors that drive microgel behavior *in vivo*

To address this gap in knowledge, this work uses poly(N-isopropylacrylamide)-co-acrylic acid (pNIPAM-AAc) microgels as a case study in how microgel crosslink density affects mechanical properties of microgels in physiologic settings, and correspondingly influences their behavior *in vivo*. The central hypothesis of this work is that increased crosslinking leads to shorter blood circulation time of microgels, and enhanced margination to the walls of blood vessels. Microgel characteristics were evaluated with a combination of single microgel atomic force microscopy (AFM) nanoindentation techniques along with light scattering and rheological analysis of microgel suspensions. A variety of microfluidic systems were used to investigate microgel behavior in whole blood, while *in vivo* testing was carried out to determine biodistribution, clearance time, and potential toxicity.

Increased crosslinking had minimal effect on clearance time and margination of pNIPAM-AAc microgels, though crosslinking was associated with longer retention time

in the kidneys. During biodistribution studies, it was observed that some mice who received crosslinked microgels showed signs of significant toxicity. Follow-up *in vitro* and *in vivo* studies revealed that crosslinked microgels have a greater tendency to form large aggregates in blood that can occlude lung microvasculature, though this does not lead to an overall inflammatory response. Instead, it is likely that crosslinked microgels occasionally form especially large aggregates that result in rare catastrophic events similar to a pulmonary embolism. Further exploration of this phenomenon revealed that aggregate formation is driven by hydrophobic interactions and exacerbated by the binding of plasma proteins such as albumin. Rational design of microgel-based therapies should utilize stably hydrophilic polymers to minimize protein binding and reduce the risk of aggregate formation in blood.

CHAPTER 1. INTRODUCTION AND SPECIFIC AIMS

Microgels, also known as nanogels, are deformable microparticles consisting of crosslinked networks of hydrophilic polymers. Due to their relative ease of synthesis and tunable features, including size, charge, stiffness, porosity, hydrophobicity, and degradation, microgels are an attractive platform for therapeutic drug delivery, imaging contrast agents, and biosensors. Yet despite a wide breadth of applications explored in published literature over the past two decades, only a couple of therapies involving microgels have reached clinical trials. The primary barriers to clinical translation of microgel-based therapies are rapid clearance *in vivo* and microgel associated toxicity or off-target effects. While there is plenty of research describing potential biological uses of microgels, there exists a critical gap in knowledge about the long-term safety of microgel therapies.

This work aims to fill that gap by using a standard microgel design as a case study. Poly(N-isopropylacrylamide) (pNIPAM) is one of the most commonly used polymers for microgel design, in part because of its unique stimuli-responsive behaviors. pNIPAM-based microgels have been synthesized with a wide range of crosslinking density using the common crosslinker N,N'-methylenebisacrylamide (BIS), resulting in varying stiffness in the final product. Additionally, pNIPAM microgels are frequently co-polymerized with acrylic acid (AAc), which adds a net negative charge and allows for simple protein ligation. But the effect of these modifications on microgel behavior *in vivo* is poorly characterized. The central question of this research is:

How does crosslink density influence the clearance time, biodistribution, and safety of pNIPAM-AAc microgels?

This question was addressed through two specific aims:

Aim 1: Determine the effect of pNIPAM-AAc crosslinking on mechanical behaviors of microgels in biologic fluids

The central hypothesis of this aim was that increased crosslinking of microgels would result in stiffer individual microgels, and that exposure to plasma would further increase the Young's modulus of microgels through the formation of a protein corona. Furthermore, I hypothesized that the increased Young's modulus of crosslinked microgels would result in enhanced margination in whole blood and higher apparent blood viscosity. These hypotheses were interrogated with atomic force microscopy (AFM) nanoindentation, dynamic light scattering (DLS), and microfluidic imaging of microgels in whole blood.

Aim 2: Establish a relationship between microgel crosslink density, aggregate formation, and pulmonary toxicity

The central hypothesis of this aim was that BIS-crosslinked microgels more readily form aggregates in blood, and that these aggregates become trapped in lung microvasculature, leading to endothelial damage and inflammation. Aggregate formation in a variety of solvents was tested using confocal microscopy, and evaluation of occlusion and toxicity was investigated in both *in vitro* microfluidic devices and *in vivo* mouse models with histology, flow cytometry, and cytokine quantification.

Broader Impacts:

Although these aims are focused on pNIPAM-AAc microgels, this thesis discusses how the results presented here can be applied to the rational design of a variety of microgel formulations. Understanding the microgel characteristics that lead to aggregation *in vivo* will help to avoid toxicity in preclinical trials and accelerate microgel-based therapies to the clinical space. Furthermore, the finding that microgels naturally accumulate in the lungs and kidneys present a unique opportunity for targeted therapeutic delivery without the need for ligation of targeting moieties.

CHAPTER 2. BACKGROUND INFORMATION

2.1 Properties of Microgels

2.1.1 What is a Microgel?

Microgels, also known as nanogels, are formed by synthesizing crosslinked hydrophilic polymer networks into micro- or nano-sized hydrogel particles. Microgels are distinguished from other nanoparticles by their ability to swell with a high volume of water relative to their total size, unlike metallic nanoparticles (e.g. gold, silver) or rigid polystyrene nanoparticles. Microgels can be synthesized from a variety of hydrophilic polymers, such as pNIPAM, PEG, poly(methyl acrylate) (PMA), and polyethylenimine (PEI), to name a few (*1*). pNIPAM-based microgels in particular have been extensively studied over the past several decades due to the relative ease of synthesis and ability to modulate size, charge, porosity, hydrophobicity, stimuli-responsiveness, and degradation kinetics through changes in reaction conditions (*2*). Microgels are mostly spherical particles, though recent advancements have demonstrated the fabrication of microgel materials of varying shapes (*3, 4*). Often, microgels are synthesized with a core-shell structure with a hydrogel "shell" surrounding a "core" that could be comprised of either another hydrogel or a different material (*2*), though other synthesis strategies have yielded microgels with hollow cores (*5*).

In addition to their biological applications, described in section 2.3, microgels have been explored for a variety of research and industrial purposes, including rheology modifiers (*6, 7*), photonic crystals (*8-12*), and responsive membrane design (*13*).

Researchers have utilized the high tunability and responsiveness of microgels to fit the needs of each application.

2.1.1.1 Crosslinking of pNIPAM Microgels

pNIPAM microgels are synthesized by a process known as "precipitation polymerization" whereby a sulfate radical initiates NIPAM monomers, which polymerize into progressively longer chains until they collapse into a colloidally unstable "precursor particle." These precursor particles then aggregate until they form a colloidally stable particle high above the lower critical solution temperature (LCST) (*14*). In order for any microgel to maintain its shape and stability in the context of other materials, individual polymer chains must be crosslinked together to form a network. Most commonly, this is accomplished by the addition of a chemical crosslinker during synthesis reactions, resulting in covalent bonds between polymer chains (*15*). However, crosslinking without a chemical crosslinker is possible, by utilizing hydrogen binding, hydrophobic interactions, or electrostatic properties of polymer chains (*16*, *17*).

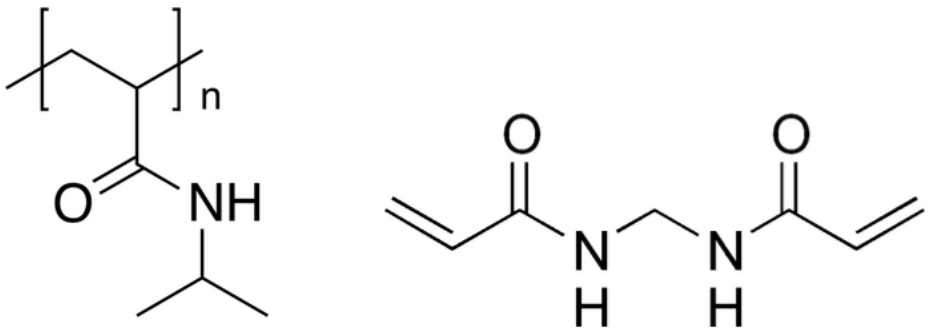

Figure 1: pNIPAM (left) and its crosslinker BIS (right). Images adapted from Wikipedia

N,N'-Methylenebisacrylamide (BIS) is widely used as an exogenous crosslinker for acrylamide-based microgels such as pNIPAM **(Figure 1)**. pNIPAM microgels can also be synthesized in a crosslinker-free reaction, which utilizes the capacity of pNIPAM chains to undergo chain transfer reactions at temperatures high above the LCST of NIPAM, resulting in self-crosslinked networks. pNIPAM microgels synthesized without an exogenous crosslinker (often referred to as "ultra-low crosslinked" or ULC) are similar to BIS-crosslinked microgels in most characteristics including size and shape, though they display lower solid content and higher swelling ratios than BIS-crosslinked microgels (*16*). ULC microgels can be fabricated with a variety of sizes, swelling ratios, and solid content by varying the temperature of the synthesis reaction, amount of NIPAM monomer, and concentration of the free-radical initiator (*18*). While both ULC and BIS-crosslinked microgels typically display diameters of approximately 1 μm in their swollen state, Lyon et al. have generated so-called "giant" ULC microgels with diameters of about 8 μm by initiating synthesis at 45 ˚C and increasing to 60 ˚C at a rate of 30 ˚C/hour (*19*).

2.1.2 Swelling Behavior of Thermoresponsive pNIPAM Microgels

At low temperatures, pNIPAM chains interact with water molecules primarily through hydrogen binding with the amide side groups of NIPAM. As temperature increases past the lower critical solution temperature (LCST), hydrogen bonding weakens, and hydrophobic polymer-polymer interactions (driven by the isopropyl groups of NIPAM) are favored. The net result of these changes is the shift in pNIPAM chain structure from random coil to collapsed globule. When this phase transition occurs over the entirety of the

polymer network comprising a microgel, water is expelled as the microgel collapses (*2*). This is commonly referred to as the volume phase transition temperature (VPTT).

The LCST of pNIPAM in water is ~32 ˚C, but this can be modulated by changing synthesis parameters or solution components. For example, acrylic acid (AAc) is often co-polymerized into pNIPAM networks to introduce carboxylic acid moieties than can be used for ligation of small molecules or proteins. AAc also gives pNIPAM microgels a net negative charge at neutral or high pH. Under these conditions, intraparticle electrostatic repulsions prevent the collapse of pNIPAM chains and stabilize the swollen conformation, effectively raising the LCST. This effect can be reversed by lowering the pH of the solvent to below the pKa of AAc, or by adding a source of cations (such as NaCl or Ca^{2+}) to shield negative charges from repelling one another. Additionally, increased osmotic pressure from solvated ions contributes to enhanced deswelling of microgels (*2, 20*). Furthermore, the degree of crosslinking can influence swelling behavior of pNIPAM microgels. Gao and Frisken showed that ULC microgels display a greater swelling ratio (measure of the difference between swollen diameter and collapsed diameter) than BIS-crosslinked microgels (*16*).

Swelling behavior is an important consideration when designing microgel-based technologies. Any biological application of microgels should take into account physiological conditions; not only is body temperature (37 ˚C) very close to the LCST of pNIPAM, but biological fluids are replete with salts, divalent cations such as calcium, and charged proteins that may influence swelling behavior. Collapsed microgels occupy a much smaller space than swollen ones, reducing their effective volume fraction within a given medium and affecting the intended use of the microgels.

2.1.3 Mechanical Properties of pNIPAM Microgels

Microgels are generally thought of as soft materials. Due to their relatively low solid content and random coil polymer chain structure, they are far more deformable than particles formed from non-hydrogel polymers such as polystyrene, or other material classes like metals and ceramics. Additionally, because the majority of a microgel's volume is comprised of the water held in its polymer network, which is expelled upon the application of force, they are classified as viscoelastic solids; i.e., their mechanical responses are time-dependent. Nonetheless, several groups have attempted to characterize the ensemble behavior of microgel suspensions, as well as the equilibrium mechanical properties of individual microgels.

Atomic force microscopy (AFM) nanoindentation allows for precise sampling of the mechanical properties of materials. Typically, AFM probes for imaging purposes are designed with a sharp, pyramidal tip with a radius of ~50 nm to grant high spatial resolution. However, these tips result in high stress on the material, often causing plastic deformation in otherwise elastic materials. For this reason, AFM tips for sampling soft materials are often modified by adding a large colloidal probe (e.g. a polystyrene bead with diameter 1-5 μm) to the end of the cantilever. Using this method, Hashmi and Dufresne measured the elastic (Young's) modulus of pNIPAM particles crosslinked with 3.5 mol% BIS throughout the phase transition. Microgels fully swollen in water at 27 ˚C displayed a Young's modulus of 13 kPa, whereas microgels past the LCST had stiffened almost an order of magnitude, to 123 kPa (*21*). Interestingly, there is a noted discrepancy in literature values for the modulus of pNIPAM microgels, even when using similar methodology. Using AFM nanoindentation as well, Tagit et al. reported in 2008 that pNIPAM microgels

crosslinked with 6.8 mol% BIS below the LCST had a Young's modulus of 1.8 ± 0.2 MPa, and stiffened to 12.8 ± 3.6 MPa after the phase transition past the LCST (*22*). While the relative difference between swollen and collapsed measurements is similar for the two studies, the absolute modulus measurements differ by two orders of magnitude; far more than could be expected to result from experimental error or the differences in crosslink density.

Obviously, the degree of crosslinking would be expected to influence microgel stiffness. ULC microgels are the least crosslinked pNIPAM microgels, and were measured by Bachman et al. using AFM nanoindentation to have an elastic modulus of approximately 10 kPa (*23*). When the same group crosslinked PEI microgels with 4% BIS, the modulus increased by an order of magnitude to about 100 kPa, though these measurements were performed on microgel films, not single microgels (*24*). Notably, all of these measurements to date have been done in simple solvents such as water or saline. To understand the mechanics of microgels used for biological applications, AFM measurements should measure how stiffness changes after microgels are exposed to protein-rich biological fluids.

It is worthwhile to ask why changes in microgel stiffness could affect biological outcomes of microgel-based technologies. Cells are uniquely sensitive to the stiffness of their underlying substrate, with differential stiffness driving simple cell behaviors such as motility and proliferation, as well as coordinated events such as differentiation and tissue morphogenesis (*25-27*). Furthermore, there is increasing evidence that the stiffness of micro- and nanoparticles regulates the manner by which they are taken up by immune cells such as macrophages. Banquy et al. found that nanoparticles with a Young's modulus of ~18 kPa were taken up by macropinocytosis, whereas stiffer particles (~200 kPa) were

internalized via clathrin-mediated endocytosis (*28*). Additionally, Merkel et al. have demonstrated that by decreasing the modulus of a red blood cell-mimicking hydrogel by 8-fold, a 30-fold increase in circulation time could be achieved (*29*). For these reasons, the mechanical properties of microgels are an important design parameter to direct *in vivo* outcomes such as clearance time, biodistribution, and immune response.

2.2 The Protein Corona and its Influence on Biological Outcomes

Any material that comes into contact with physiological fluids is subject to fouling by proteins, and micro/nanoparticles are no exception. Upon intravenous injection, plasma proteins interact with the surface of the particle, adsorbing through non-covalent binding such as hydrophobicity, charge, hydrogen binding, and van der Waals forces. The resulting layer of proteins is referred to as a protein "corona," and its composition is dynamic. Initially, a "soft" corona of weakly bound proteins surrounds the particle, which over time is replaced by higher-affinity proteins that form a "hard" corona on the surface of the particle (**Figure 2**). For many micro/nanoparticles, the corona is largely comprised of albumin, the most abundant serum protein. However, less common proteins such as fibrinogen, plasminogen, immunoglobulins, and apolipoproteins have been identified in protein coronae, sometimes in greater amounts than their proportional concentration in serum would suggest (*30*).

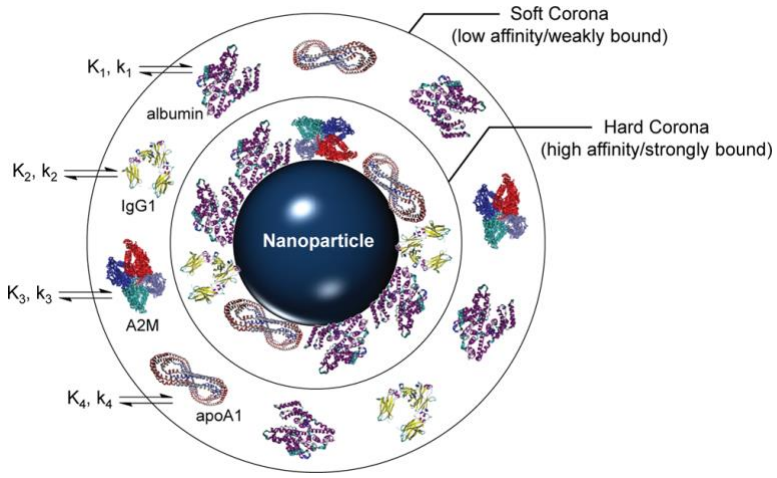

Figure 2: Example of protein corona formation on a nanoparticle surface. Protein adsorption is dynamic and dependent on the affinity of individual proteins to the nanoparticle surface as well as other proteins. Figure from Fleischer and Payne, 2014 (*30*).

2.2.1 The Role of the Protein Corona in Determining In Vivo *Fate*

The behavior of micro/nanoparticles in blood circulation is a critical determinant of their efficacy and safety. As with any biomaterial, micro/nanoparticles are recognized by the body's immune system as foreign objects, and are typically taken up by the mononuclear phagocyte system (MPS, consisting of dendritic cells, blood monocytes, and macrophages) following injection. In addition to reducing the effective dose of particles in circulation, MPS uptake is correlated with enhanced inflammation and toxicity (*31*, *32*).

Cells interact with biomaterials through the proteins bound to their surface before they encounter the material itself. Adsorbed proteins bind receptors (e.g. Mac-1) on the surface of phagocytic cells that regulate particle binding and internalization (*33*-*36*). Both quantitative and qualitative changes in the protein corona can influence their interactions with the MPS. In general, more bound protein of any type leads to greater immune cell binding and particle internalization, reducing the effective dose and half-life of nanoparticles in circulation (*37*, *38*). However, recent work has demonstrated that the

specific serum proteins adsorbed could have differing effects on MPS uptake. Nanoparticles coated with human serum albumin appear more likely to be phagocytosed, whereas those coated with immunoglobulins show less uptake, even after being re-introduced to whole plasma (*39, 40*).

2.2.2 Effect of Micro/Nanoparticle Design Parameters on Protein Corona Formation

Since the corona is responsible for mediating *in vivo* behavior of micro/nanoparticles, several groups have investigated how design parameters of a variety of micro/nanoparticle systems influences corona formation and composition. A common method to reduce protein adsorption to the surface of nanoparticles (and subsequent MPS uptake) is to surround them with PEG, which has a low affinity for most plasma proteins (*41, 42*). Several groups have found that increasing the molecular weight and surface density of PEG on the surface of nanoparticles results in even lower protein adsorption, though blocking corona formation completely remains challenging (*43, 44*).

Polystyrene nanoparticles are used for a wide variety of research, therapeutic, and imaging applications, and can be synthesized with several different surface chemistries. Gessner et al. found that surfaces with acidic functional groups (which carry a negative charge at physiologic pH) preferentially bind proteins with an isoelectric point (pI) > 5.5, and vice versa. Correspondingly, the authors observed that when compared to particles with acidic functional groups, those with basic functional groups (e.g. NH_2) bound greater amounts of albumin, which is negatively charged at physiologic pH (*45*). These results indicate that micro/nanoparticle-protein interactions are strongly influenced by electrostatic forces.

The protein corona is sensitive not only to changes in particle design, but also the forces experienced by the nanoparticle after injection. The Payne group has recently found that the shear forces experienced by nanoparticles in flow can influence the composition of the resulting protein corona. Increased flow rate was associated with greater total protein content, and specifically enhanced binding of plasminogen, a precursor to the fibrinolytic enzyme plasminogen. Furthermore, fluorescence and circular dichroism spectroscopy revealed structural changes in plasminogen in response to flow, suggesting partial denaturation of the protein. Additionally, cellular binding to protein-nanoparticle complexes was found to be significantly reduced on nanoparticles exposed to flow (*46*). These results demonstrate the sensitivity of the protein corona to physiologic shear forces, and stress the importance of conducting protein corona research in settings that accurately model those conditions.

A simple method to modify the protein corona is pre-incubation with a desired protein or set of proteins. Müller et al showed that pre-treating polystyrene nanoparticles with plasma depleted of human serum albumin and immunoglobulins reduced the likelihood of aggregation when added to whole plasma (*39*). In a related study, it was demonstrated that pre-coating with immunoglobulin-depleted plasma decreases cellular uptake by immune cells (*40*). By understanding which proteins are responsible for adverse events such as aggregation and cellular uptake, nanoparticles can be pre-coated to avoid these behaviors.

2.2.2.1 The Protein Corona of Thermoresponsive pNIPAM Microgels

Until recently, little was known about the corona of thermoresponsive pNIPAM microgels. Research has indicated that pNIPAM has low nonspecific plasma protein adsorption (*47*). However, Cedervall et al demonstrated that pNIPAM-co-N-tert-butylacrylamide nanoparticles bound human serum antigen initially, which was replaced by higher affinity apolipoproteins AI, AII, AIV, and E (*48*). Additionally, Miceli et al. have recently characterized the corona of pNIPAM microgels using dynamic light scattering (DLS) and protein mass spectrometry (MS). Overall, they found that albumin and Apolipoprotein B-100 (ApoB100) were the primary corona proteins in all pNIPAM microgels studied. An important caveat to this research is that the pNIPAM microgels in this study were crosslinked with 33% dendritic polyglycerol (dPG), which enhances the hydrophilicity of the overall polymer network, effectively raising the LCST beyond body temperature. The authors state that this modification is critical to prevent hydrophobic collapse of the pNIPAM microgel upon intravenous injection. For comparison, control particles of pNIPAM crosslinked with 4% BIS were included in the analysis. Coronae from microgels synthesized with dPG were found to contain higher relative amounts of apolipoproteins such as ApoB100 and haptoglobin (HPT), although pNIPAM microgels without dPG (which were collapsed at 37 ˚C) bound a greater total amount of protein.

Notably, Miceli et al also compared the propensity of pNIPAM microgel formulations to aggregate in the presence of serum. All pNIPAM microgel formulations displayed aggregate intensity fractions of less than 30%, and the presence of dPG was found to completely inhibit aggregate formation at 25 ˚C (below the LCST). dPG-pNIPAM microgels also showed temperature-dependent aggregation. When incubated with serum at 37 ˚C, dPG-pNIPAM formed aggregates that were significantly reduced upon cooling to

25 ˚C. The authors note that the partial collapse of dPG-pNIPAM microgels at 37 ˚C led to enhanced adsorption of immunoglobulin (IgG) light chains, and link this event to the reversible formation of aggregates (*49*).

Taken together, these results point to an important characteristic of pNIPAM microgels: the composition of their protein corona, and their corresponding likelihood to aggregate in circulation, is dependent on their swelling state. Microgels that are fully swollen bind less protein, and specifically less aggregation-inducing IgG molecules. Microgels that are in a hydrophobic state, and thus partially or fully collapsed, have more protein-rich coronae and aggregate more readily. Notably, there is a lack of understanding of the influence of microgel crosslinking on protein corona formation and subsequent aggregation.

2.3 Biomedical Applications of Microgels

2.3.1 Microgel-based Strategies to Modulate Hemostasis

Due to their micron-range size and similar softness to blood cells, microgels make excellent candidates for tissue engineering strategies to emulate platelets and treat hemostatic disorders. The Barker lab is actively involved in the development of platelet-mimetic microgel particles to treat bleeding from thrombocytopenia, or low platelet count. These so-called platelet-like particles (PLPs) consist of a ULC 95% pNIPAM/5% AAc microgel particle functionalized with a fibrin-specific single-domain antibody fragment (sdFv), termed H6. H6 was screened from a library of sdFv clones using phage display, and was designed to bind fibrin over its circulating precursor fibrinogen. This specificity endows PLPs with a unique targeting ability; in theory, PLPs circulate passively in the

bloodstream until they encounter a nascent fibrin clot, whereupon they bind and stabilize the clot in a manner similar to native platelets. Notably, PLPs are capable of initiating clot collapse, mimicking clot contraction by native platelets, a behavior not observed in other synthetic platelet technologies. It is likely that the extraordinary deformability and stimuli-responsiveness of ULC microgels enables this behavior. Most importantly, PLPs were found to significantly reduce bleeding time in an *in vivo* rat femoral vein injury model, as well as enhance clot formation in several *in vitro* systems (*50*). Recently, Sproul et al. have found that PLPs formed from hollow microgels with lightly crosslinked shells initiate fibrin clot collapse to a greater degree than PLPs made from microgels with traditional core-shell structures, supporting the hypothesis that microgel deformability is critical for clot collapse (*5*).

Building on this foundation, several groups have designed fibrin-targeting microgel-based therapies with the opposite goal: inhibiting coagulation and destabilizing fibrin clots. Kodlekere and Lyon recently reported on a poly(N-isopropylmethacrylamide) (pNIPMAM) microgel conjugated to the peptide GPRPFPAC, which mimics the fibrin knob 'A.' These microgels successfully disrupted the polymerization of stable fibrin clots, presumably through competitive binding to the holes 'a' of the fibrin molecule, a key step in the formation of a stable fibrin mesh (*51*). Furthermore, Mihalko et al. have developed a complex microgel system in which fibrin targeting antibodies on the microgel core direct the particle to existing fibrin clots. Once bound to fibrin, the microgels release both tissue plasminogen activator (tPA, which initiates fibrinolysis) and the small molecule cell contractility inhibitor Y-27632. This dual delivery system was shown to enhance blood flow and reduce cardiac fibrosis *in vivo* following myocardial infarction (*52*).

2.3.2 Microgels for Therapeutic Delivery

Biological molecules and drugs can be loaded into microgels through covalent attachment to polymer chains, or using non-covalent forces such as hydrophobic interactions, van der Waals, or electrostatic forces. Because of their low solid content as a percentage of their total volume, microgels can hold 30% of their weight or more in therapeutic cargo. This capacity is greater than that of liposomes and polymeric micelles, and makes microgels ideal carriers for therapeutic delivery (*53, 54*). Loading microgels with small molecules or drugs often triggers collapse of the polymer network in a manner similar to the volume phase transition of thermoresponsive microgels (*1*). While this may encourage aggregation, it also presents an opportunity to design drug release systems that work in tandem with the stimuli-responsive nature of many microgel systems.

2.3.2.1 Delivery of Small Molecules

One of the most straightforward methods for loading small molecule therapeutics into microgels is by designing microgels with the opposite charge to the target molecule. This can be easily accomplished by co-polymerizing charged monomers into the microgel polymer network. For example, as discussed earlier, AAc can be incorporated into pNIPAM microgels to generate negatively-charged particles at physiologic pH. Alternatively, positively charged PEG-polyethyleneimine (PEG-PEI) microgels have been generated to carry common biologically active compounds such as retinoic acid, indomethacin, or valproic acid. Importantly, these loaded microgels formed stable colloidal suspensions and were able to by lyophilized and resuspended while still maintaining function (*55, 56*).

In order to contain charged groups and control the distribution of cargo within a microgel, Kim et al generated PEG-*b*-poly(methacrylic acid) (PEG-b-PMA) which contain an anionic PMA core surrounded by a hydrophilic PEG shell. These microgels were capable of carrying up to 50 weight% of the common chemotherapy agent doxorubicin (DOX), which is weakly cationic. Furthermore, due to their anionic core, the PEG-b-PMA microgels exhibited enhanced release in acidic pH, a hallmark of tumor microenvironments. By adding disulfide-bonded crosslinks to the PMA core, the authors created microgel carriers that can be degraded on-demand by the addition of a reducing agent (*57*).

Microgels also offer a method to enhance the delivery of drugs that are poorly soluble in water, due to their tunable hydrophilicity. Wang et al. loaded paclitaxel (PTX), another common chemotherapy agent, into chitosan-poly(NIPAM-co-acrylamide) nanogels and demonstrated temperature-dependent release of the drug. Furthermore, PTX-loaded microgels had higher anti-tumor efficacy than delivery of free PTX (*58*). Another group utilized microgels formed from lauryl-modified dextran and β-cyclodextrin to carry benzophenone, a highly hydrophobic chemical used in sunscreen. By solubilizing benzophenone in the dextran and β-cyclodextrin polymer solutions prior to forming microgels, the authors created carriers with up to 2.5 weight% benzophenone, which is normally completely insoluble in water (*59*).

2.3.2.2 Delivery of Therapeutic Oligonucleotides

Oligonucleotides (including small interfering RNAs (siRNAs), micro RNAs (miRNAs), and antisense oligodeoxynucleotides (ODNs)) have been a topic of great

interest in recent years, as they offer a new modality for treating diseases ranging from cancer to viral infections. However, due to their negative charge, it is difficult for oligonucleotides to penetrate cell membranes and perform their designated function (*1*). Cationic microgels are an obvious vehicle to enhance oligonucleotide delivery, and there have been multiple reports confirming the feasibility of this approach.

In one of the first examples of this strategy, Vinogradov and coworkers loaded cationic PEG-PEI microgels with antisense phosphorothioate ODN targeting the human mdr1 gene, which encodes for P-glycoprotein, involved in mediating drug-drug interactions. Delivering microgel-bound ODN inhibited the production of P-glycoprotein to a significantly greater degree than delivery of the ODN by itself (*60*). In recent years, researchers have developed a wide variety of cationic microgel formulations that allow for optimal oligonucleotide loading and delivery (*61, 62*).

2.3.2.3 Delivery of Protein Therapeutics

Proteins and peptides present unique delivery challenges due to their rapid clearance, large size compared to small molecules or oligonucleotides, limited stability, and potential for off-target effects. Once again, microgels are promising carriers because of their high loading capacity and ability to protect their cargo from degradation. Proteins can be passively adsorbed to microgels through hydrophobic or electrostatic interactions, which can stabilize hydrophobic proteins that would normally aggregate in aqueous solutions. However, upon injection, therapeutic proteins must compete with plasma proteins for the same binding sites. As a corona forms over injected microgels, therapeutic proteins can be lost (*1*).

Several groups have developed strategies to overcome this limitation. Hasegawa et al. designed "raspberry-like" assemblies of multiple cholesterol-modified pullulan-based microgels by crosslinking with thiol-modified tetra-armed PEG. These assemblies demonstrated efficient encapsulation of interleukin-12 (IL-12) and delivered a stable dose of IL-12 for 72 hours following subcutaneous injection (*63*). Nagahama and coworkers encapsulated lysozyme into self-assembled poly-(L-lactide)-grafted dextran microgels, and were able to achieve sustained release of active lysozyme for up to a week while avoiding initial burst release upon injection (*64*).

Another method to control the release of the therapeutic protein is to take advantage of natural environmental cues such as pH and oxidative stress. In one example of this strategy, lysozyme was loaded into acid-labile microgels formed from inverse emulsion polymerization of N-vinylformamide with a ketal-containing crosslinker. At pH 5.8, about 95% of the encapsulated lysozyme was released, compared to only 15% at pH 7.4 (*65*). To exploit the reducing environment inside cells, Chen et al. used reversible addition fragmentation chain transfer (RAFT) to polymerize disulfide crosslinked microgels composed of PEG-*b*-poly(2-(hydroxyethyl) methacrylate-co-acryloyl carbonate), which were used for triggered intracellular release of loaded proteins (*66*).

Cationic cholesterol-bearing pullulan (cCHP) microgels have also been investigated as an antigen-delivery system for adjuvant-free vaccines. Non-toxic subunit fragments of Clostridium botulinum type-A neurotoxin (BoHc/A) were encapsulated into cCHP microgels and administered intranasally. Loaded cCHP microgels were able to pass through mucus and bind to the nasal epithelium, where BoHc/A was taken up by mucosal dendritic cells (*67*). cCHP microgels have since been tested as vaccine carriers in clinical

trials for therapy-refractory HER-2 positive breast cancer (*68*), esophageal cancer (*69*), and malignant melanoma (*70*).

2.3.3 Imaging and Diagnostics

In a manner similar to their ability to hold and deliver small molecules and proteins, microgels make excellent candidates for carrying imaging probes and contrast agents. Loading magnetic nanoparticles (e.g. iron oxide) into microgels prior to administration enhances both colloidal stability and magnetic resonance imaging (MRI) sensitivity over delivery of magnetic nanoparticles alone (*71, 72*). Furthermore, microgels can encapsulate a large quantity of magnetic nanoparticles, leading to a stronger local magnetic field (*73, 74*). In a fascinating study, Okada et al. demonstrated that crosslinked PMA-based microgels function as MRI pH sensors by themselves, obviating the need for inorganic magnetic contrast agents. This surprising property is based on the collapse of PMA microgels at acidic pH, resulting in the restriction of water molecules interacting with polymer chains and a corresponding decrease in transverse relaxation time (*75*). Furthermore, microgels have been employed to mitigate toxicity from common small molecule MRI contrast agents such as gadolinium (*76*) as well as silver or gold nanoparticles (*77, 78*).

Microgels can also be loaded with radiotracers for use in positron emission tomography (PET) imaging. By crosslinking polyacrylamide-based microgels with polydentate chelating ligands such as 1,4,7,10-tetraazacyclododecane-1,4,7,10-tetraacetic acid (DOTA), the Almutairi group generated scaffolds for metal radionuclides such as ^{64}Cu. When injected into a mouse model of metastatic cancer, ^{64}Cu-DOTA-based nanogels

accumulated in both the primary tumor and metastases, with minimal off-target accumulation in the liver or spleen (*79*). Microgel-based PET probes can also be designed to be stimuli-responsive, as Singh et al. demonstrated with reduction-sensitive partially thiolated poly(ethylene oxide-*stat*-polypropylene oxide)-based microgels that chelate ^{68}Ga (*80*).

Near-infrared (NIR) imaging is the ideal fluorescence-based imaging modality for *in vivo* applications due to strong penetration of the signal through tissue and limited autofluorescence. However, the only approved NIR probe for clinical imaging is indocyanine green (ICG), which degrades quickly in aqueous media, has a low quantum yield, and self-quenches at sufficiently high concentration (*81*). To address these issues, and exploit the intrinsic properties of ICG, poly(β-amino ester) (PBAE) nanogels were developed with CD44 receptor-targeting hyaluronic acid to sequester ICG in a self-quenched (i.e. non-fluorescent) state until they reach their target site. Upon receptor-mediated endocytosis by cancer cells, the pH sensitive PBAE is degraded, slowly releasing ICG and resulting in a fluorescent signal (*82*). Similar hyaluronic acid-containing nanogels have also been used to monitor hyaluronidase activity *in vivo*, a hallmark of cancer metastasis and angiogenesis (*83*). One particularly clever application of NIR probe-loaded microgels involved the use of multiple sizes of IRDye800-loaded cholesterol-modified pullulan (NIR-CHP) microgels to visualize cancer metastasis to regional lymph nodes. When injected to a primary tumor site, NIR-CHP probes with diameters >300 nm stayed in the primary tumor, whereas NIR-CHP probes with diameters 10 and 50 nm were taken up into the sentinel lymph node (SLN). Meanwhile, the smallest probes (diameters 5-10

nm) flowed through the SLN into adjacent nodes, allowing for complete imaging of lymphatic metastasis (**Figure 3**) (*84*).

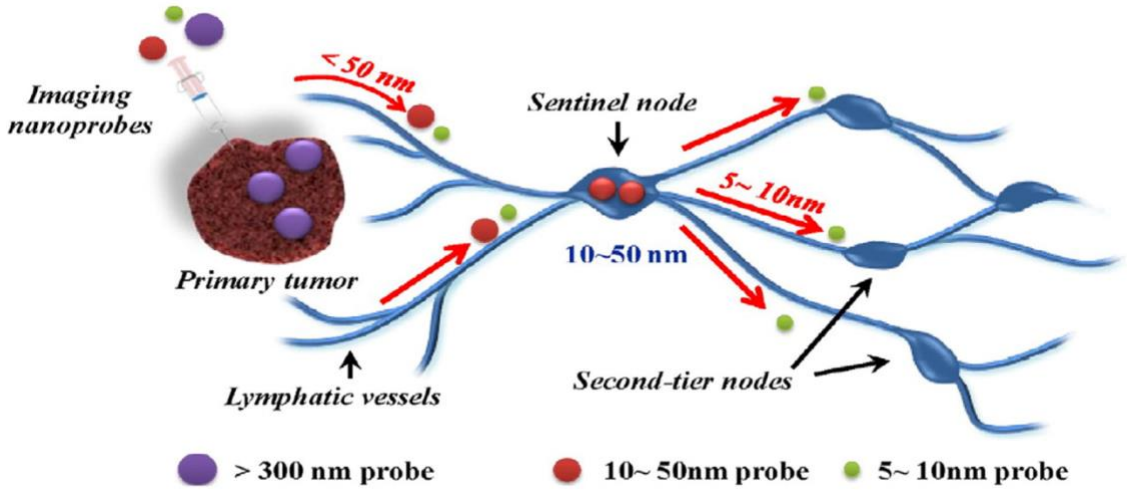

Figure 3: Imaging metastasis through lymph nodes with NIR-CHP microgel probes of varying diameter. Figure adapted from Noh et al. (*84*).

In addition to imaging applications, microgels can be used to enhance the stability and sensitivity of enzyme-based electrochemical biosensors for diagnostic purposes. Due to their ease of synthesis and ability to hold a large cargo of active enzymes, microgels have been designed to sense choline (*85*, *86*), phenol (*87*), blood esterases (*88*), and organophosphates (*89*).

2.3.4 Barriers to Clinical Translation of Microgels

Despite the significant advancement in our understanding of microgel behaviors, and the wide breadth of biomedical applications explored over the past several decades, there are vanishingly few microgel-based therapies or diagnostics in the clinical space. With the notable exception of cCHP microgels used for antigen delivery, no microgel technologies have been investigated in clinical trials. Most of the key reasons for this can

be grouped into two broad categories: rapid clearance, and toxicity/off-target effects. For a more comprehensive overview of barriers to microgel translation, the reader is directed to an excellent review by Soni et al. (*1*).

2.3.4.1 Rapid Clearance

The body is equipped with a number of systems to remove foreign material from circulation. Like most micro- or nanomaterial therapies, a primary concern is that on average, only 5-10% of the injected dose is actually delivered to the target site, due to clearance from kidneys, liver, spleen, etc. (*90*, *91*). Splenic filtration is responsible for removing microgels over ~200 nm in diameter (*92*), whereas the kidneys may excrete smaller microgels directly through renal filtration (*93*, *94*). In addition to size, the shape of microgels has been demonstrated to influence circulation time, with spherical microgels cleared more rapidly than filamentous or rod-shaped microgels (*95*). Furthermore, Merkel et al. showed that by decreasing the modulus of red blood cell-mimicking microgels by a factor of 8, they could extend the circulation time by 30-fold, suggesting that microgel stiffness is an important determinant of circulation time (*96*). As discussed in section 2.2.2, the composition and robustness of a protein corona on the surface is also correlated with enhanced opsonization and uptake by the MPS system. While incorporating hydrophilic polymers such as PEG can reduce opsonization and extend clearance time, it should be noted that PEG is not completely inert; antibodies to PEG are generated after a single dose, which results in faster clearance and reduced efficacy upon subsequent dosing (*97-99*). Finally, it is known that microgels with neutral charge circulate for longer than charged microgels (*100, 101*). However, since many microgel designs are dependent on charged

moieties for stimuli-responsive behavior and loading of drug cargo, it is difficult to completely mitigate charge-dependent clearance.

2.3.4.2 Toxicity and Off-target Effects

Ultimately, the primary barrier to clinical translation of microgel-based technology is unforeseen toxicity. While there are many studies demonstrating the potential efficacy of microgel-based therapeutics or diagnostics, there is a critical need for research into associated toxicity and strategies to avoid it. Some known toxicity is related to properties of the microgel particles themselves. For example, in addition to accelerating clearance, positive charge on microgels is associated with cell shrinkage, formation of vacuoles, hemolysis and cell cycle disturbance (*102*). Loading cationic microgels with negatively charged cargo such as nucleic acids can shield cells from deleterious effects, but upon delivery of the cargo, the microgel once again displays positive charge.

Even without specifically targeting blood components, microgels may suffer from hemocompatibility issues. Naeye et al. showed that positively charged siRNA-loaded dextran nanogels induce platelet aggregation and bind to other blood cells, whereas negatively charged microgels did not (*103*). Negatively charged alginic aldehyde-gelatin microgels were also shown to be safe with respect to platelet aggregation and hemolysis, buttressing the argument that cationic charge leads to problems with hemocompatibility (*104*).

Microgels are also prone to aggregation in blood, which can result in severe vascular toxicity. Miceli et al. showed that BIS-crosslinked pNIPAM-based microgels with a diameter of approximately 250 nm in water can form aggregates in excess of 1 μm

diameter in serum (*49*). Considering that microvasculature in the lung, kidneys, spleen, and liver can be as small as 6 μm in diameter (*105*), these multi-microgel aggregates are close to a size that could occlude blood vessels, potentially resulting in vascular endothelial damage and inflammation, or even oxygen/nutrient deprivation in surrounding tissue. Deshmukh et al. exploited these properties to design stabilized PEG microgel aggregates to specifically target lung microvasculature on the basis of capillary diameter (*106*). While their preliminary safety data is promising, it raises a critical question: what margin of error separates safe lung targeting from something resembling a pulmonary embolism? As discussed in Section 2.2.2.1, aggregation appears to be linked to the composition and size of the protein corona, suggesting that strategies to control corona formation could enhance the safety profile of microgels in circulation.

Another source of toxicity is the potential for off-target effects from microgel formulations. A common strategy to target microgels to specific tissues or cells involves conjugating antibodies or receptor-specific ligands to the surface of the microgel. However, targeting is never fool-proof, for a variety of reasons. For one, cell surface receptors are rarely, if ever, completely exclusive to the target cell. As an example, folate receptor is overexpressed on numerous cancer cell types, but is also present on the surface of cells in the small intestine and kidneys (*107, 108*). Additionally, antibodies and other therapeutic proteins are sensitive to conformational change, and their targeting or therapeutic effects can be hindered by physical processes during microgel synthesis (e.g. shear forces from mixing) or chemical alterations such as pH and crosslinking (*109-112*).

The PLPs described in Section 2.3.1 offer another illustration of the difficulty to accurately target specific proteins. The conjugated antibody fragment that bestows their

functionality, H6, was designed to bind fibrin over its circulating precursor, fibrinogen. However, H6 still possesses a moderate affinity for fibrinogen (*50*) – could it bind enough fibrinogen to nucleate micro-emboli in circulation? Furthermore, hemostasis is a dynamic process, balancing coagulation and clot degradation to prevent bleeding or excessive thrombogenesis (*113*). PLPs may disrupt this delicate balance by stabilizing fibrin clots that would normally have been dissolved, resulting in an enhanced risk for stroke or pulmonary embolism. Future studies are needed to elucidate the safety of these and similar microgel formulations.

In summary, microgels offer a nearly limitless platform for biomedical innovation, yet very little microgel-based technology has actually made it to patients. Although there is a wealth of studies reporting proof-of-concept microgel-based therapies and diagnostics, research on the longer-term effects of microgels *in vivo* is lacking. Stated bluntly, we simply don't know enough about how microgels behave in the body, and why. The central aim of this thesis is to explore the link between microgel crosslinking and *in vivo* toxicity to inform the rational design of microgel-based biotechnology.

CHAPTER 3. EFFECT OF CROSSLINK DENSITY ON MECHANICAL BEHAVIORS OF PNIPAM-AAC MICROGELS IN BIOLOGICAL FLUIDS

3.1 Abstract

Crosslinked microgels have been synthesized with a wide variety of polymers for a plethora of biological applications. Poly(N-isopropylacrylamide) (pNIPAM)-based microgels, for instance, are commonly crosslinked with N,N'-Methylenebisacrylamide (BIS). But while it has long been understood in hydrogel material science that increased crosslinking yields stiffer gels, there is a lack of consensus on the mechanical characterization of individual microgels. To address these discrepancies and build on the work performed by other groups, I have developed a robust atomic force microscopy (AFM)-based method for sampling the mechanical response of individual pNIPAM-co-acrylic acid (pNIPAM-AAc) microgels deposited on glass without interference from the underlying substrate. Furthermore, I utilize variations of this method to report, for the first time, calculation of the Young's, shear, and bulk moduli of pNIPAM-AAc microgels swollen with human plasma, to recapitulate their *in vivo* environment. As expected, all moduli increase with increasing crosslink density. Exposure to plasma generally increases the moduli of microgels, though this result is inconsistent and most pronounced in highly crosslinked microgels. Unexpectedly, microgels did not marginate to the walls of blood vessels, regardless of crosslink density. Additionally, the crosslink density of microgels was found to not influence bulk blood viscosity. In total, though crosslink density affects the stiffness

of individual microgels, these differences do not affect larger scale mechanical behaviors of microgels in blood at common doses, such as viscosity and margination.

3.2 Introduction

It has long been known that the Young's modulus of pNIPAM-based microgels can be enhanced by increasing the crosslink density. Research from the Lyon group investigated the Young's modulus of films of ULC pNIPAM and 4% BIS-crosslinked PEI microgels, and yielded moduli of 10 kPa and 100 kPa, respectively (*23, 24*). While these measurements are useful for understanding relative differences in stiffness between microgel films, their applicability to individual microgel properties is limited, since films can contain 3-4 layers of microgels deposited on top of one another. Despite these findings and others, detailed analysis of single microgel mechanical properties, including characterization of shear and bulk moduli, is lacking. Furthermore, there have been no reports on the changes in mechanical properties that occur when microgels are immersed in blood plasma, which closely recapitulates their eventual environment for *in vivo* applications.

Notably, two studies have undertaken single-microgel AFM nanoindentation with vastly differing results, as discussed in Section 2.1.3. Hashmi et al. found that pNIPAM particles crosslinked with 3.5% BIS had a Young's modulus of 13 kPa when swollen in water below the LCST, and these particles stiffened to 123 kPa when swollen with water heated past the LCST (*21*). By contrast, Tagit et al. reported that pNIPAM microgels crosslinked with 6.8 mol% BIS below the LCST had a Young's modulus of 1.8 ± 0.2 MPa, which increased to 12.8 ± 3.6 MPa after heating past the LCST (*22*).

This work aims to resolve the discrepancies in our understanding of single microgel mechanical properties, and build on this foundation by measuring bulk and shear modulus for these materials in a variety of solvents. I hypothesized that incubation with plasma results in an increase in Young's, bulk, and shear moduli as a result of protein adsorption and microgel deswelling.

In addition to analyzing the mechanical properties of single microgels, this work aimed to analyze the effect of microgels on the viscosity of blood, known as hemorheology. Blood is a complex, non-Newtonian fluid composed of a solid, cellular phase (red blood cells (RBCs), white blood cells, platelets) suspended in an aqueous solution of proteins, lipids, and salts called plasma. Blood is characteristically shear-thinning, meaning that apparent viscosity decreases with increasing shear. This is due to the aggregation of RBCs. At low shear, RBCs form reversible multicellular aggregates known as rouleaux (**Figure 4A**). RBC aggregates disturb flow streamlines to a greater extent than single RBCs, resulting in a higher apparent viscosity. As flow rate increases, these aggregates break up in a shear-dependent manner, causing a decrease in the apparent viscosity. At even higher shear, there are practically no rouleaux, and the continued decrease in viscosity can be attributed to the high deformability of individual RBCs under shear (**Figure 4B**) (*114*).

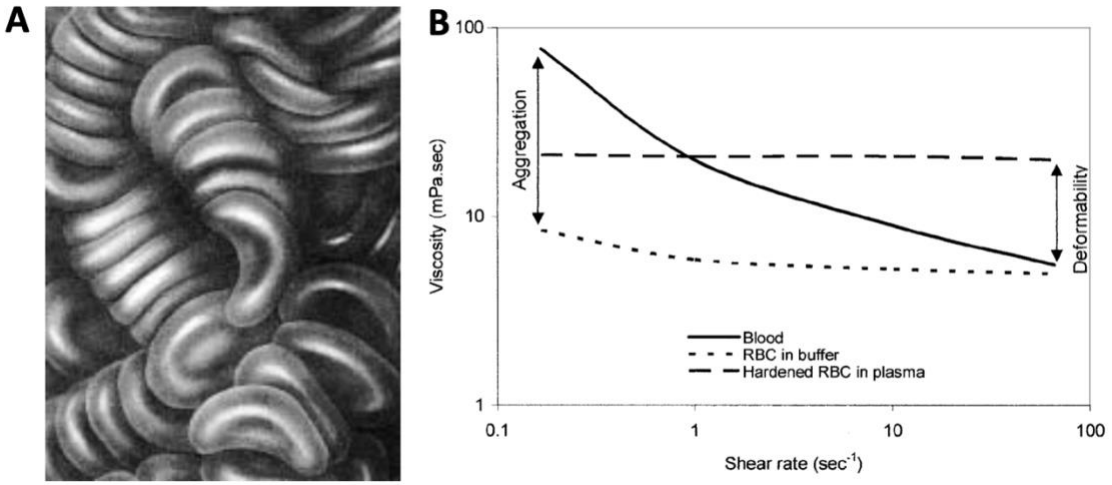

Figure 4: Basics of hemorheology. At low shear, RBCs form multicellular aggregates known as rouleaux (**A**). As shear increases, RBC aggregates break up, resulting in a lower apparent viscosity. At even higher shear, individual RBC deformability accounts for a further decrease in viscosity (**B**). Figure from Baskurt et al. (*114*).

Early *in vivo* studies with pNIPAM-AAc microgels indicated pulmonary toxicity of crosslinked pNIPAM-AAc microgels, and *in vitro* models of lung microvasculature suggested resistance to flow in these conditions, described in detail in Section 4.4. Based on these observations, I hypothesized that crosslinked microgels enhance the apparent viscosity of blood at high shear, potentially by interacting with RBCs and decreasing their deformability. In this chapter, I directly measured the viscosity of blood mixed with microgels of varying crosslink density at the *in vivo* concentration where toxicity was observed.

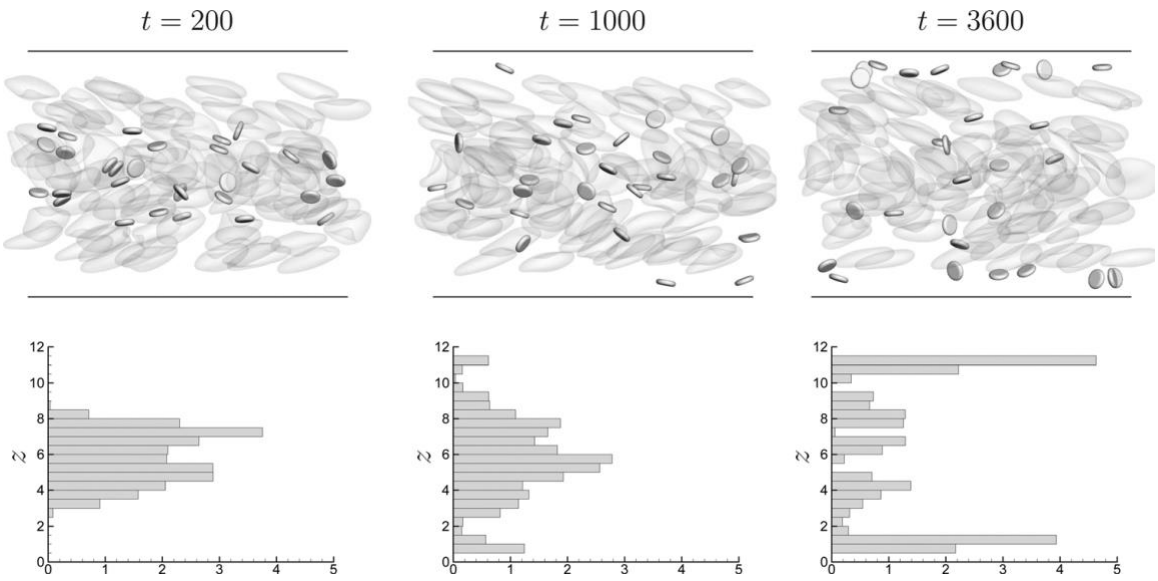

Figure 5: Simulation of platelet margination. As flow develops, soft RBCs cluster toward the center of the vessel due to lift velocity generated by the shear gradient, described by the Fahraeus-Lindquist effect. Platelets do not experience the same lift velocity due to their greater stiffness, and collide with RBCs, which push them to the margins. Figure from Zhao et al. (*115*).

Margination is a behavior of certain blood components, including platelets and leukocytes, that influences the distribution of blood cells along the diameter of the blood vessel. In order for platelets to engage with a blood vessel injury and interact with other components of hemostasis, they must be present at a high concentration immediately adjacent to the endothelial cell layer of the vessel wall. Native platelets accomplish this through a process called margination. High shear flow (such as that experienced in microcirculation) causes deformable red blood cells (RBCs) to generate a lift velocity away from the wall of the vessel, resulting in an RBC-free layer known as the Fahraeus-Lindquist effect. Platelets are about an order of magnitude more rigid than RBCs, and thus do not exhibit the same behavior. Additionally, the comparatively rigid platelets colliding with deformable RBCs in flow introduces a shear-induced diffusion of platelets from the RBC-rich region. The net effect is that platelets end up trapped in the RBC-free layer near the

vessel wall, as seen in **Figure 5** (*115-117*). I hypothesized that microgel margination could be enhanced by increasing the crosslink density of microgels, resulting in a higher effective dose of microgels at the vessel wall. Using a particle tracking algorithm in a microfluidic channel, I analyzed the degree to which microgels of varying crosslink density marginate in whole blood.

3.3 Materials and Methods

3.3.1 pNIPAM-AAc Microgel Synthesis

The synthesis protocol for pNIPAM-based microgels is reviewed in detail in other publications (*14, 16, 118*). Briefly, NIPAM (Sigma Aldrich) was recrystallized in hexane prior to use. Acrylic acid (AAc) (VWR), ammonium persulfate (APS) (ThermoFisher), and BIS (Sigma Aldrich) were all used as received. 100 mL of deionized water was added to a clean 250 mL round bottom flask using a filtered syringe. The water was stirred at 650 rpm throughout the synthesis procedure. 1.8 g of NIPAM was dissolved in 20 mL of deionized water and added to the reaction flask through a filtered syringe. BIS was also added at this step if synthesizing exogenously crosslinked microgels. N_2 gas was bubbled through the solution as it heated to 70 ˚C. AAc was diluted in 1 mL of deionized water prior to addition to the reaction through filtered syringe for a final concentration of 5 mol%. After 10 minutes of mixing, the N_2 needle was lifted over the solution to create a blanket of N_2 over the reaction. To initiate, 36 mg of APS was dissolved in 4 mL of deionized water and added to the reaction through a filtered syringe. Initiation was confirmed by visual observation of increasing opacity of the solution, changing from clear to light blue to milky white within 2-3 minutes. The reaction was run overnight, maintaining temperature at 70 ˚C. After

allowing the reaction to cool, large aggregates were filtered out using glass wool, and the microgels were purified by dialysis against deionized water with a 30 kDa molecular weight cutoff membrane. Microgels were lyophilized for long-term storage.

3.3.2 Immobilizing Microgels on Coverslips

12 mm diameter glass coverslips were cleaned according to the following protocol: 20 minute bath sonication in deionized water with Alconox detergent (Sigma Aldrich), 15 minute bath sonication in deionized water, 15 minute bath sonication in acetone, 15 minute bath sonication in absolute ethanol, 15 minute bath sonication in absolute isopropyl alcohol (IPA). Cleaned coverslips were stored in absolute IPA prior to use. To prepare for microgel deposition, coverslips were placed in wells of a 24-well plate and dried with compressed air. Coverslips were then silanized by adding 0.5 mL of 1% (v/v) (3-Aminopropyl)trimethoxysilane (Sigma Aldrich) in absolute ethanol to each well and incubating for 1 hour at room temperature. Wells were washed once with absolute ethanol and three times with deionized water. Microgels were suspended in deionized water at a concentration range of 0.01-0.001 mg/mL and 0.5 mL of each suspension was added to the cleaned, silanized coverslips in the well plate. Microgels were left to deposit passively overnight at room temperature, before being rinsed three times with deionized water to remove unbound microgels. Prepared coverslips were left hydrated in deionized water for up to 1 month after functionalization to avoid artifacts from drying/rehydrating cycles.

3.3.3 AFM Tip Calibration

Silicon nitride AFM cantilevers were purchased with a 1 μm diameter polystyrene bead attached to the end of the tip (Novascan). The nominal spring constant of the tips used

for these studies was 0.02 N/m. The tip was calibrated at the beginning of each experiment according to the following procedure: After submerging the tip in the solvent used for that experiment, the tip was allowed to equilibrate to temperature until the deflection stayed constant for several minutes. A single force measurement against glass was then taken, from which the deflection inverse optical level sensitivity (DefInvOLS) and virtual deflection line were measured. The tip was then raised away from the surface of the glass, and thermal fluctuation data was gathered to complete the spring constant calibration in Asylum software (Oxford Instruments).

3.3.4 Single Microgel Force Mapping

Microgel-coated coverslips were submerged in the desired solvent, and both the coverslip and the AFM tip were allowed to equilibrate to temperature. Unless otherwise specified, measurements were taken at 25 ˚C. Next, a 10 μm by 10 μm force map was created in tapping mode with a 450 pN trigger force, 750 nm force distance, and 1.8 Hz scan rate. Individual microgel particles were located from this map, and an appropriate x-y offset was selected to move the tip to a single microgel, which was imaged with a 2 μm by 2 μm force map with the same parameters.

3.3.5 Generation of Force vs. Indentation Curves

After obtaining a force map of a single microgel, the "nudger" feature was used to move the AFM tip to the center of the microgel particle. A macro was built in Asylum to perform a number of different indentations. First, trigger force was held constant at 350 pN while approach velocity was increased from 2 μm/s to 12 μm/s, in 2 μm/s increments. Next,

approach velocity was held constant at 2 μm/s, with an added three second "dwell" after indentation. The trigger force was then decreased from 350 pN to 110 pN in 40 pN increments. Four measurements were taken for each set of parameters.

3.3.6 Calculation of Young's, Shear, and Bulk moduli

Calculation of mechanical properties was based primarily on the Hertz model of contact between two spheres (Equation 1), where F is force, R_c is the radius of curvature of the tip, ν is the Poisson ratio of the microgel, *E* is the Young's modulus, and δ is the indentation depth of the tip. Importantly, the Hertz model is only accurate for synthetic gels for small deformations (strain < 0.05), so indentation depth was carefully monitored throughout all measurements (*119*).

$$F = \frac{4\sqrt{R_c}}{3}\frac{E}{1-\nu^2}\delta^{\frac{3}{2}} \quad (1)$$

To solve for shear modulus (G), it was necessary to use the elastic conversion formula in Equation 2, where K is bulk modulus:

$$E(K,G) = \frac{9KG}{3K+G} \quad (2)$$

The shear measurements were performed at sufficiently high velocity to avoid deswelling of the microgel, determined empirically by taking shear measurements at increasing velocity, shown in **Figure 6.**

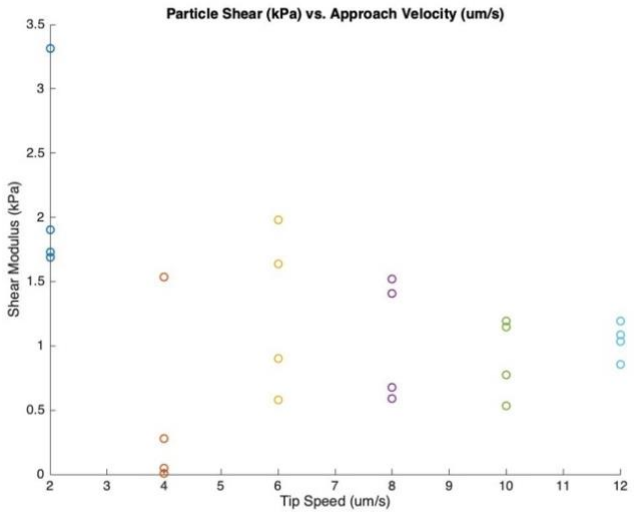

Figure 6: Representative graph of measured shear modulus vs AFM tip speed for one 8% BIS microgel swollen in water. For each speed, four measurements were taken. After an initial decrease in measured modulus from 2 μm/s to 4 μm/s, the modulus levels out up to 12 μm/s. The tip speed selected for measuring shear was the highest speed for which a measured force vs. indentation slope had an acceptable goodness of fit ($R^2 > 0.9$).

Because of this, I assume that the material is incompressible, i.e. K → ∞. Taking the limit of Equation 2 as K→∞ results in the expression E = 3G, as shown in Equation 3:

$$\lim_{K\to\infty} \frac{9KG}{3K+G} = 3G \tag{3}$$

If I assume that the material is incompressible, I can also set the Poisson ratio ν = 0.5. Taken together, these substitutions result in the Equation 4 used to calculate G. By raising the known indentation depth δ to the 2/3 power, and calculating the slope of the resulting force versus modified indentation curve at low indentation depth, G can be solved for each measurement. A representative set of data used for this analysis can be seen in **Figure 7.**

$$F = \frac{4\sqrt{R_c}}{3}\frac{3G}{1-0.5^2}\delta^{\frac{3}{2}} \tag{4}$$

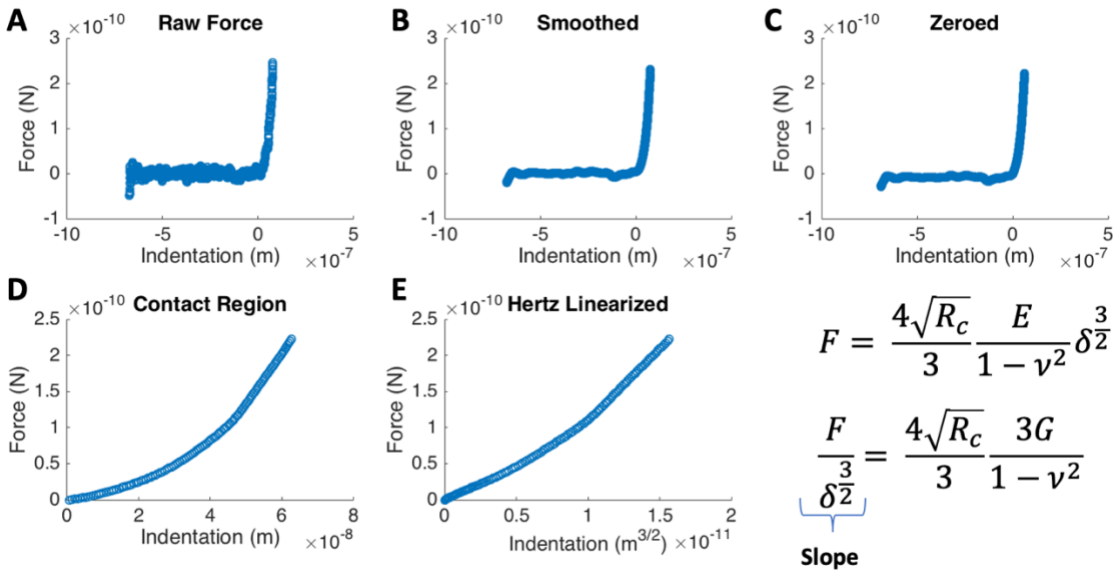

Figure 7: Analysis of shear modulus for a representative microgel. **A,** the raw force vs. indentation curve exported from the AFM software. **B,** the curve was smoothed with a radius of 80 data points to reduce thermal noise from the AFM tip. **C,** the curve was zeroed at the contact point, determined by the AFM software and corrected by visual interpretation of each curve. **D,** magnified view of the contact region. **E,** contact region force vs. indentation linearized by raising the indentation to the 3/2 power, as per the Hertz model. Note the "kink" in the force curve about halfway through indentation, indicating that the Hertz model no longer applies. For this reason, all measurements were taken from the slope measured in the early, linear region of the curves.

A similar method can be used to calculate bulk modulus, though the interpretation of the force versus indentation curve is more complex. For these measurements, the tip was "dwelled" at increasing trigger points for 3 seconds, and the resultant force at the end of the dwell curve was read as the force at that specific indentation. For most dwell curves, the relaxation from the initial indentation was on the order of milliseconds (**Figure 8B**).

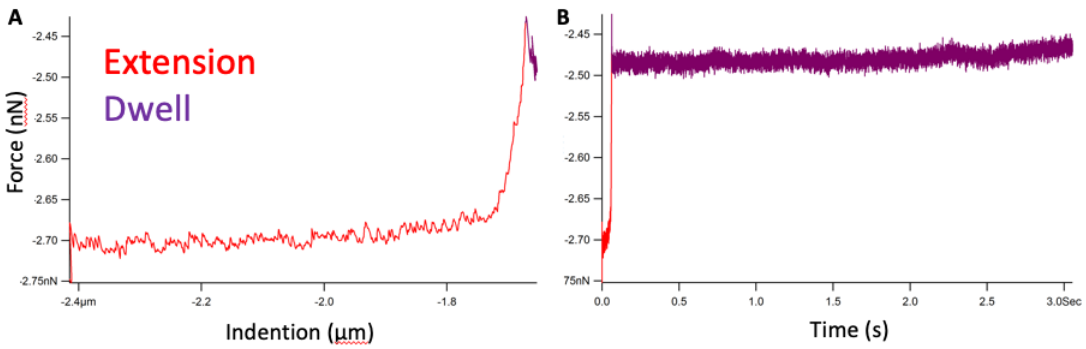

Figure 8: Example of a dwell force curve. **A**, Force vs indentation. **B**, Force vs. time. The initial extension is shown in red, and the dwell is shown in purple.

The force versus indentation curve was then manually constructed from these points. Additionally, since the microgel was deswelling, and thus compressing, ν could no longer be set to 0.5. Instead, the elastic conversion formula for ν in terms of K and E was used (Equation 5), since E was already known for each particle from the shear measurements described above.

$$\nu(K,E) = \left(\frac{3K - E}{6K}\right) \tag{5}$$

This expression was substituted back into Equation 1 to yield the following Equation 6, used to solve for K. A representative set of data used for this analysis can be seen in **Figure 9.**

$$F = \frac{4\sqrt{R_c}}{3}\frac{E}{1 - \left(\frac{3K - E}{6K}\right)^2}\delta^{\frac{3}{2}} \tag{6}$$

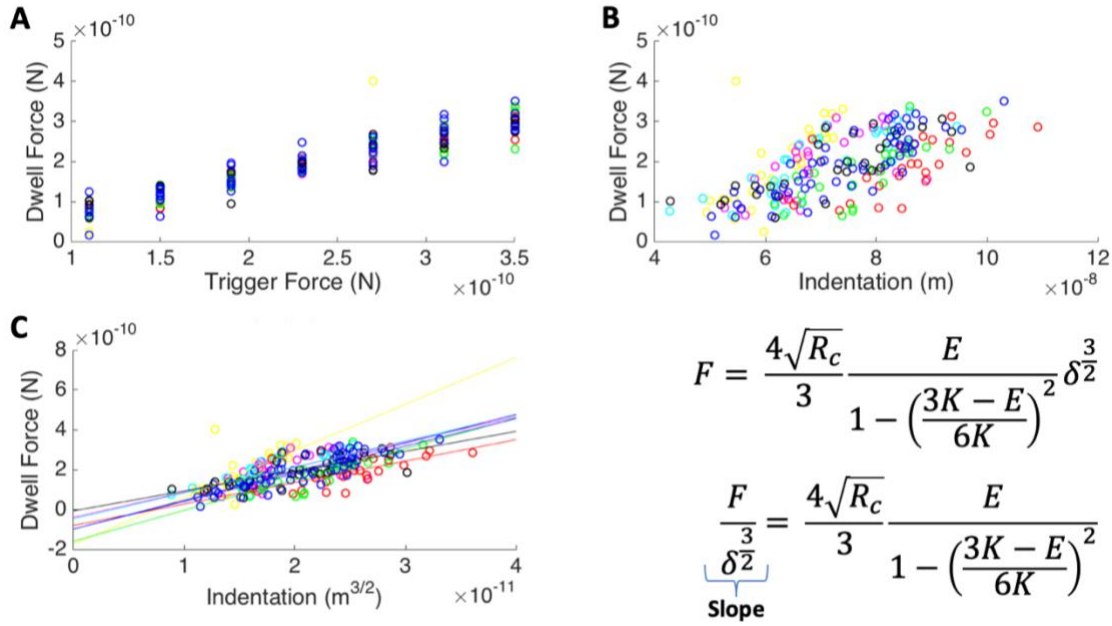

Figure 9: Analysis of bulk modulus for a representative set of microgels (each microgel is a different color curve). **A,** measured force at the end of 3 seconds of dwelling on each microgel vs. the set trigger point. **B,** the same force data, plotted against the measured indentation at the trigger points in **A. C,** Force vs Hertz-linearized indentation, showing slope fit for each microgel.

3.3.7 Dynamic Light Scattering Measurements of Microgels

Microgels were suspended in various solvents at a dilute concentration (0.01 mg/mL). Laser scattering was measured using a 3D dynamic light scattering instrument (LS Instruments) and analyzed with a custom-built MATLAB script from the Fernandez-Nieves lab to extract hydrodynamic radius for each microgel species. More details on analysis of light scattering can be found in a previous publication by Sierra-Martin et al. (*120*).

3.3.8 Calculation of Volume Fraction

Volume fraction represents the amount of space taken up by a particular species compared to the total volume of the sample. Normally, it is calculated using Equation 7, where ϕ is

volume fraction, $N_{particles}$ is the number of particles in the sample, $V_{swollen}$ is the volume of one particle at its maximum swollen state, and V_{total} is the total volume of the sample.

$$\phi = \frac{(N_{particles})(V_{swollen})}{V_{total}} \tag{7}$$

However, since the number of particles (or in this case, microgels) is particularly difficult to quantify due to the near-transparent nature of swollen pNIPAM microgels, a different calculation is required. The mass concentration of microgels can be determined gravimetrically, i.e. by weighing out larger quantities of lyophilized microgels (> 5 mg) and adding a known volume of solvent. An ideal expression would relate the resulting mass per volume concentration (mg/mL) to volume fraction. Toward this goal, we can utilize what we know about the mass of microgels added, described in Equation 8, where m_{solid} is the mass of microgels added, $V_{collapsed}$ is the volume of one microgel completely collapsed (i.e., not swollen with solvent), and ρ is the density of NIPAM (1.1 g/cm^3).

$$m_{solid} = (N_{particles})(V_{collapsed})(\rho_{NIPAM}) \tag{8}$$

Solving for the unknown $N_{particles}$ and substituting back into Equation 7 yields the following Equation 9 that relates mass per volume to volume fraction. The central term ($V_{swollen}/V_{collapsed}$) is commonly referred to as the "swelling ratio" and can be determined by DLS measurements of microgel size at varying swollen states.

$$\phi = \left(\frac{m_{solid}}{V_{total}}\right)\left(\frac{V_{swollen}}{V_{collapsed}}\right)\left(\frac{1}{\rho_{NIPAM}}\right) \tag{9}$$

There are a few caveats to the above analysis which should be noted. For one, the exact mass of microgels added to the solvent can be difficult to measure precisely – even when working with masses > 5 mg, the accuracy of the balance used to measure may vary by ± 0.1 mg, as per the Mettler Toledo website (www.mt.com). Furthermore, the density term only accounts for the density of NIPAM. Since all microgels in this analysis contain 5 mol% AAc (density 1.05 g/cm^3), and some contain BIS (density 1.24 g/cm^3), the actual density of each sample may vary slightly. But since NIPAM makes up the vast majority of the polymer network, and the densities of AAc and BIS are similar to that of NIPAM, these differences are likely negligible. By far, the most important source of uncertainty in calculating volume fraction with Equation 9 is the swelling ratio. While DLS can provide accurate size measurements of microgels in various solvents, a true swelling ratio would relate the size of microgels swollen in blood, complete with plasma as well as cellular components, to their dry state. The measurements reported cannot replicate these exact conditions, and thus the volume fractions should be interpreted as a close estimate, and viewed in relation to one other instead of as an absolute determination.

3.3.9 Hemorheological Analysis of pNIPAM-AAc Microgels in Whole Blood

Blood was drawn into sodium citrate to prevent coagulation, and mixed with microgels at a concentration of 1 mg/mL. 4 mL of the blood mixture was loaded into an Anton-Paar rheometer. Rotational shear rate ranging from 0.01 to 10,000 s^{-1} was applied to the mixture, and the resultant viscosity was analyzed for each shear rate.

3.3.10 Evaluation of pNIPAM-AAc Microgel Margination in Whole Blood

To assess the degree to which pNIPAM-AAc microgels marginate to the edges of blood vessels, Cy3b-labeled microgels of varying crosslink density were mixed with citrated whole blood at an approximate concentration of 200,000 microgels/μL, to mimic the concentration of native platelets. The mixed blood was then perfused through a 150 μm wide x 150 μm tall straight microfluidic channel at a physiologic shear of 1 dyne/cm^2. A custom-written MATLAB code (in collaboration with Meredith Fay from the Lam lab) was used to count the individual microgels and track their location within the channel from confocal microscopy videos. In certain experiments, native platelets were labeled with an antibody against CD41 (Novus Biologics) to compare against platelet margination.

3.4 Results

3.4.1 Young's, Shear, and Bulk moduli of pNIPAM-AAc Microgels

The summary of AFM nanoindentation modulus measurements for ULC, 2% BIS, and 8% BIS microgels is shown in **Table 1**. To assess the changes in mechanical properties upon immersion in physiologic liquids, measurements were collected after swelling microgels with either deionized water (DI H_2O), phosphate-buffered saline (PBS), or human blood plasma.

Table 1: Summary of AFM nanoindentation experiments on pNIPAM-AAc microgels of varying crosslink density. Young's (*E*), shear (*G*), and bulk (*K*) moduli were calculated as described in section 3.3.6. N ≥ 5 microgels for each condition, with the median of 4 measurements being calculated for each individual microgel. Data is reported as mean ± standard deviation.

***E* (kPa)**		**ULC**	**2% BIS**	**8% BIS**
	DI H_2O	2.71 ± 1.74	10.87 ± 4.31	9.91 ± 4.96
	PBS	2.79 ± 1.28	7.34 ± 1.56	7.65 ± 2.59
	Plasma	5.63 ± 1.40	8.26 ± 1.99	22.64 ± 10.74
***G* (kPa)**		**ULC**	**2% BIS**	**8% BIS**
	DI H_2O	0.90 ± 0.58	3.62 ± 1.44	3.30 ± 1.65
	PBS	0.93 ± 0.43	2.45 ± 0.52	2.55 ± 0.86
	Plasma	1.88 ± 0.47	2.75 ± 0.66	7.55 ± 3.58
***K* (kPa)**		**ULC**	**2% BIS**	**8% BIS**
	DI H_2O	0.37 ± 0.25	1.56 ± 0.72	1.31 ± 0.70
	PBS	0.36 ± 0.16	1.03 ± 0.29	0.99 ± 0.39
	Plasma	0.77 ± 0.18	1.11 ± 0.31	3.52 ± 1.95

The modulus measurements displayed high variability, as reflected in the standard deviations reported. As expected, ULC pNIPAM-AAc microgels were the softest measured in all moduli, regardless of solvent. Microgels crosslinked with 2% BIS exhibited an approximately 4-fold increase in stiffness when swollen with deionized water. Increasing the crosslink density further to 8% had a negligible effect on modulus measured in deionized water or PBS. Comparing similar microgels swollen with either deionized water or PBS, it seems that ULC microgels are agnostic to the increased salt concentration of PBS. BIS-crosslinked microgels appear to soften slightly when swollen with PBS, but this

is not significant (ANOVA, Tukey's posttest). Swelling with human plasma greatly enhances the measured moduli of ULC and 8% BIS-crosslinked microgels, but has minimal effect on 2% BIS-crosslinked microgels. In total, the bulk moduli of all microgels was lower than their respective shear moduli, indicating that compressing pNIPAM-AAc microgels requires less force than shearing them.

3.4.2 Height Profiles of pNIPAM-AAc Microgels on Glass

While gathering force versus indentation measurements for pNIPAM-AAc microgels, AFM force maps of individual microgels were also obtained. These maps are contain height information on microgels deposited on glass, though not in the usual contact mode that is employed when generated height maps with AFM. Instead, each "pixel" of the image is a single indentation of the tip, and records the height at which the set trigger force was reached. By normalizing the height information of force maps of various microgels, we can gather a relative comparison of microgel shape after swelling with different solvents, as seen in **Figure 10**.

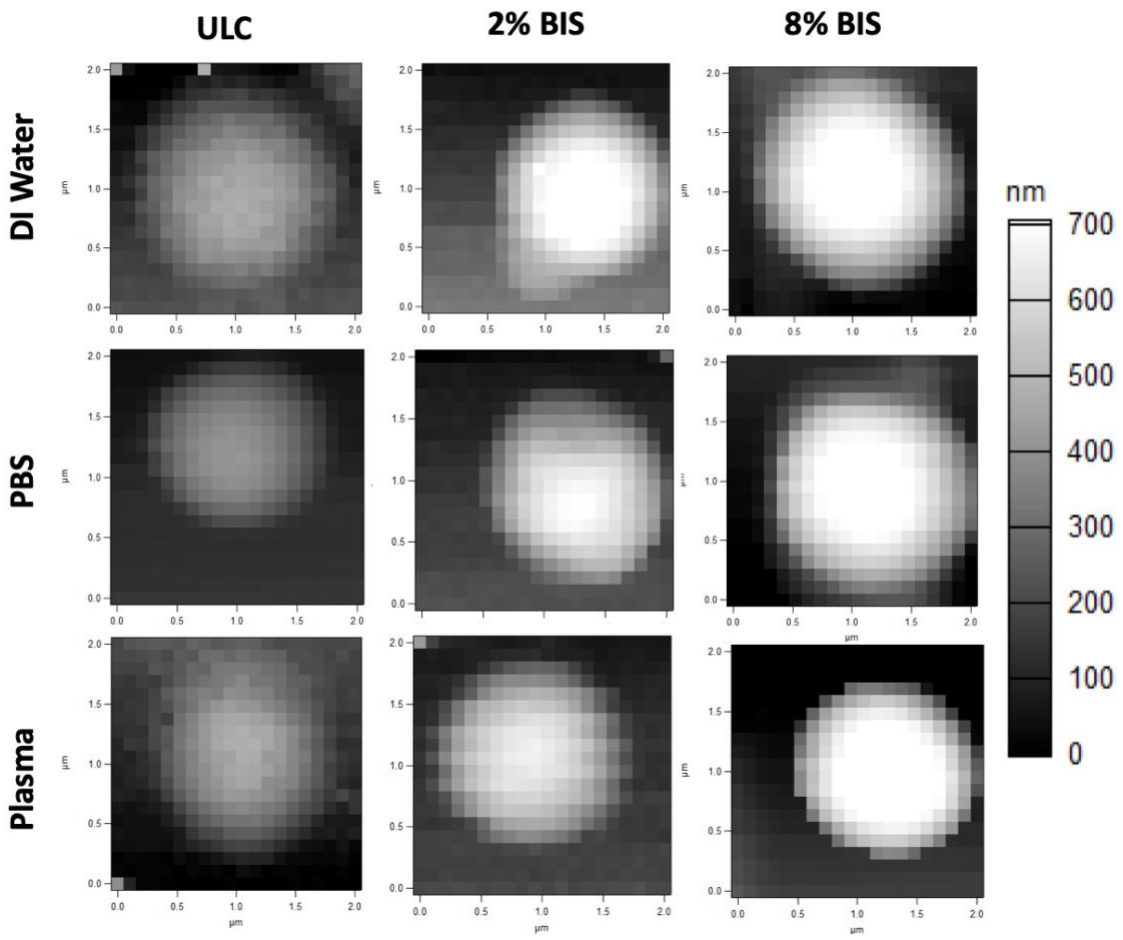

Figure 10: Height profiles of individual pNIPAM-AAc microgels of increasing crosslink density immobilized on glass and swollen with various solvents. Height information was obtained through force maps of individual microgels, where each pixel is one indentation.

ULC microgels immobilized on glass spread to a diameter of approximately 1.5 μm when rehydrated in deionized water, and reach a maximum height of about 300 nm. Their diameter is slightly less in PBS or plasma, though their height remains the same. Microgels crosslinked with 2% BIS maintain a diameter of slightly over 1 μm in all solvents, and swell to a height between 600 and 700 nm. Microgels crosslinked with 8% BIS show a more similar morphology to microgels crosslinked with 2% BIS than to ULC microgels, though they maintain a greater height, with most microgels reaching at least 700 nm above the glass surface. 8% microgels also have a much more clearly defined edge between the

microgel and surrounding glass, whereas 2% BIS microgels, and particularly ULC microgels, show a more gradual transition from microgel to glass. This difference is especially pronounced in the 8% BIS microgels swollen with plasma. These morphological distinctions reflect the differences in internal structure of pNIPAM-AAc microgels that arise from increasing crosslink density, and the rigid boundary observed with 8% BIS microgels swollen with plasma suggests changes in the way that these microgels form a protein corona when exposed to blood plasma.

3.4.3 Swelling Behaviour and Volume Fraction of pNIPAM-AAc Microgels

In order to predict the behavior of microgels *in vivo*, it is necessary to understand how they swell in response to various environmental conditions. Beyond providing information about size, pNIPAM microgel swelling behavior is indicative of the hydrophobicity of the polymer chains that comprise the microgel (*2*). The most straightforward way to measure microgel swelling behavior is through DLS analysis of microgel size with varying solvents and temperatures. Ideally, microgel size in whole blood should be interrogated; however, the opacity of blood due to the presence of other suspended objects such as cells precludes this analysis. Instead, two conditions were designed to mimic the "collapsed" and "swollen" states of the microgels. For the "collapsed" condition, pNIPAM-AAc microgels were suspended in deionized water with 150 mM NaCl, pH 3, at 60 ˚C. The NaCl encourages collapse of the microgels through osmotic pressure, and the pH of 3 is below the pKa of acrylic acid (pKa 4.2), ensuring that the vast majority of acrylic acid groups are protonated and therefore not ionized. Finally, raising the temperature of the solution to 60 ˚C places the microgels well above their volume phase transition temperature (VPTT). For the "swollen" state, microgels were suspended in phosphate buffered saline at 37 ˚C. It is

important to note that these conditions are not indicative of the maximum swollen state of pNIPAM-AAc microgels. For maximum swollen size, microgels should be suspended in deionized water at pH 9, where their acrylic acid groups are ionized, thus stabilizing the swollen conformation through intraparticle charge repulsion. Additionally, to observe microgels in their fully swollen state, their temperature should be lowered to well below their VPTT, such as 15 ˚C. But for these studies, we are interested in studying microgels as swollen as they would be in physiologic settings. **Table 2** shows the size measurements of pNIPAM-AAc microgels of varying crosslink density in collapsed and physiologically swollen states, as well as their swelling ratios.

Table 2: Hydrodynamic radius (R_h) of pNIPAM-AAc microgels in collapsed and physiologically swollen states, as measured by DLS. Data is reported as mean ± standard error. The swelling ratio was calculated by dividing the physiologically swollen volume (V_s) by the collapsed volume (V_c), assuming a spherical shape.

	ULC	2% BIS	8% BIS
Physiologically Swollen R_h (nm)	810 ± 48	442 ± 18	379 ± 11
Collapsed R_h (nm)	690 ± 18	376 ± 7	333 ± 11
Swelling ratio (V_s/V_c)	1.62	1.62	1.47

ULC microgels display a larger hydrodynamic radius (R_h) than BIS-crosslinked microgels in both collapsed and physiologically swollen states, and R_h decreases monotonically with the degree of crosslinking. All microgels exhibited significant collapse upon suspension in acidic solution above the VPTT, as reflected in the swelling ratio (V_s/V_c). However, microgels crosslinked with 8% BIS had a slightly lower swelling ratio, indicating a lesser degree of collapse than microgels with lower crosslink density. This

might suggest that the high crosslink density of 8% BIS microgels confers a resistance to collapse in physiologic conditions.

Preliminary biodistribution and clearance time experiments, discussed in detail in Section 4.4, were modeled after hemostasis studies with fibrin-targeting microgels developed as synthetic platelet-like particles. The peak blood concentration ranged from 1-1.5 mg/mL, and this was used as a reference concentration for most of the *in vitro* and *in vivo* experiments throughout this work. It is useful to calculate the volume fraction of microgels in blood resulting from this concentration, both to understand the relative space the microgels occupy and to investigate whether changes in swelling behavior between microgels of different crosslink density result in different volume fractions while holding mass concentration the same. **Table 3** shows the approximate volume fractions calculated for each microgel type based on the swelling behavior in **Table 2**.

Table 3: Approximate volume fraction of microgels of varying crosslink density at 1 mg/mL.

At 1 mg/mL	ULC	2% BIS	8% BIS
Φ	0.0015	0.0015	0.0013

While 8% BIS microgels have a slightly lower volume fraction that ULC or 2% BIS microgels, owing to their lower swelling ratio, the difference is nearly negligible compared to the miniscule volume fraction occupied by all microgels. Regardless of crosslink density, it is abundantly clear that at this mass concentration, the pNIPAM-AAc microgels occupy a vanishingly small percent of the total volume of blood upon injection and mixing. Even at 10 times the injected dose, the microgels would take up less than 2% of the volume of blood.

As mentioned previously, an ideal calculation of volume fraction would be based on DLS measurements of microgel size in whole blood, or at least blood plasma, in order to include the effects of plasma protein binding. Unfortunately, DLS measurements of microgels suspended in filtered plasma were inconclusive. The only condition where there DLS analysis yielded reliable results were for the 8% BIS microgels at 14 ˚C, where an R_h of about 150 nm was detected. For all other microgel conditions, and even for plasma alone, the light scattering was dominated by a species with an R_h of approximately 60 nm. Since this was detected in plasma by itself, it is likely that this is simply particulate matter in plasma that was too small to be filtered out.

3.4.4 Hemorheology of pNIPAM-AAc Microgels in Whole Blood

To assess whether pNIPAM-AAc microgels affected the bulk viscosity of human blood at relevant *in vivo* concentrations, microgels of varying crosslink density were mixed with whole blood and measured over a range of shear rate with a rheometer. **Figure 11** shows the viscosity results ranging from a shear rate of 0.01 s^{-1} to 10,000 s^{-1}.

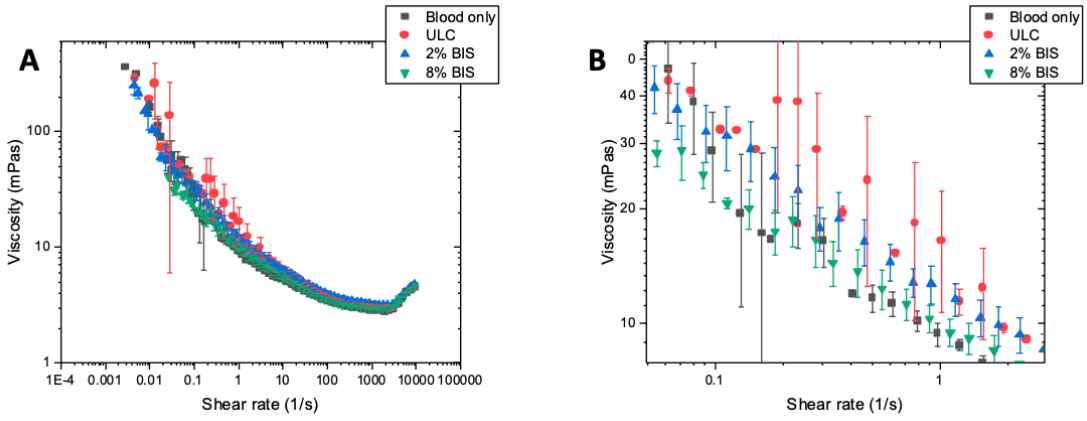

Figure 11: Rheological analysis of apparent blood viscosity vs applied shear rate for various microgel conditions. **A,** full range of shear rates from 0.01 s^{-1} to 10,000 s^{-1}. **B,** zoomed in results for 0.1 s^{-1} to 1 s^{-1}. Data presented as mean ± standard error, N = 3.

Overall, pNIPAM-AAc microgels at 1 mg/mL had minimal, if any, effect on the apparent bulk viscosity of blood over a range of physiologically relevant shear rates. **Figure 11B** shows that from 0.1 s^{-1} to 1 s^{-1}, ULC microgels potentially increase the apparent blood viscosity, though this effect was highly variable between experiments and not significant. In all conditions, blood showed characteristic shear-thinning behavior until approximately 2000 s^{-1}, at which point the apparent viscosity began to rise again. This occurred even with whole blood without any microgels. However, since this shear rate is outside the normal range of physiologic shear, it is likely that the apparent rise in viscosity is due to destruction of red blood cells, known as hemolysis (*114*).

3.4.5 Margination of pNIPAM-AAc microgels in whole blood

Preliminary studies of ULC and 2% BIS-crosslinked pNIPAM-AAc microgels suggested that 2% BIS microgels may marginate more effectively than ULC microgels, ostensibly due to their greater shear modulus. To test this effect, margination studies in whole blood were carried out with ULC, 2%, and 8% BIS-crosslinked microgels, as well as with labeled human platelets. Blood was mixed with the microgels, and perfused through a straight microfluidic channel (150 μm tall by 150 μm wide) at physiologic wall shear of 1 dyne/cm^2. The results, plotted as a histogram of microgel or platelet locations along the width of the channel, are shown in **Figure 12**.

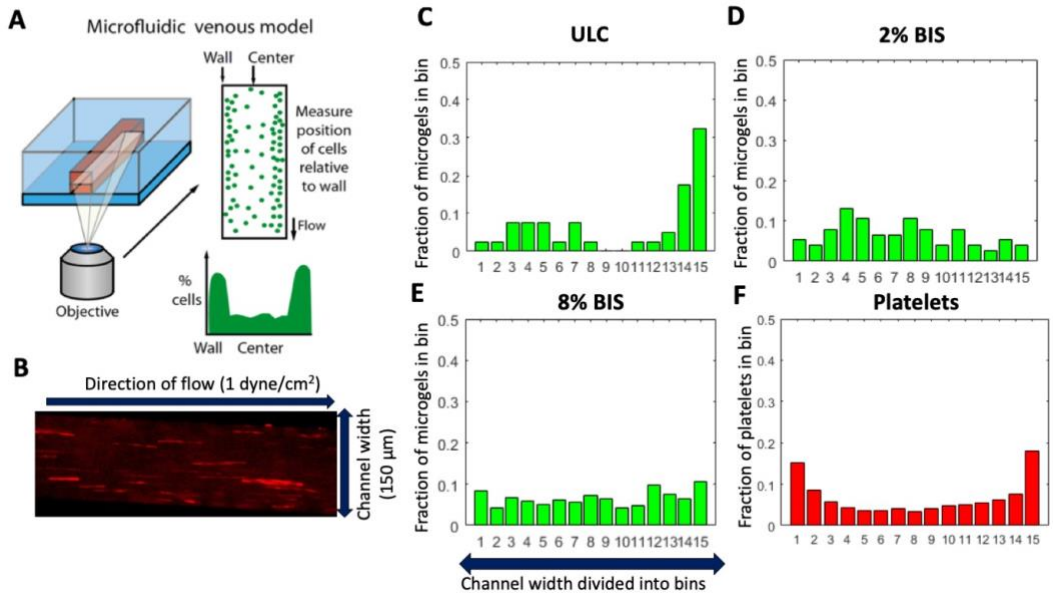

Figure 12: Representative results of margination studies with pNIPAM-AAc microgels and human platelets. **A,** schematic of microfluidic margination experimental setup (adapted from (*121*)). **B,** Labeled example of fluorescent particles flowing through the microfluidic channel. **C-F,** histogram results of microgel or particle locations across width of microfluidic channel.

Figure 12F demonstrates that human platelets marginate to the walls of the microfluidic channel as expected. However, all microgel conditions studied were highly variable, and very few showed any consistent margination behavior. The potential margination toward the wall with ULC microgels in **Figure 12C** was primarily due to adhesion to the wall of the microfluidic channel, and was not true margination.

3.5 Discussion

3.5.1 Interpretation of Single-microgel Mechanical Properties and Swelling Behavior

Prior to this work, AFM studies on the mechanical properties of individual microgels were limited, in part due to concern over the influence of the underlying substrate on measured mechanical properties (*23*). Furthermore, groups that have measured single

pNIPAM microgels with AFM through the VPTT have arrived at drastically different values, as discussed in Section 3.2. The work in this thesis was not focused specifically on probing changes in microgel mechanics throughout the VPTT, but yielded results with swollen microgels in water that are much closer to those of Hashmi et al. Furthermore, the methods employed here to ensure linearity of force vs indentation after application of the Hertz model, and the careful selection of force curves to limit analysis to only the first 20-40 nm of indentation depth, minimizes the risk of substrate influence, i.e. sampling the glass underneath the microgels.

The results presented here show that pNIPAM-AAc microgels, regardless of crosslink density, do not measurably stiffen when swollen with deionized water vs. PBS **(Table 1)**. In fact, BIS-crosslinked microgels appear to *soften* slightly with the addition of the ions from PBS, though this result is not significant. This is somewhat surprising, since the addition of salts from PBS is expected to promote microgel collapse, both by shielding the intraparticle electrostatic repulsions from negatively charged AAc groups, and inducing osmotic pressure (*20*). A possible explanation is that even with the added ions of PBS, the VPTT of the microgels is still above the range of temperatures studied here (25-37 ˚C), meaning that the microgels have not yet begun to collapse.

When exposed to human plasma, ULC and 8% BIS microgels exhibit an approximate 2-fold increase in modulus when compared to those swollen in water or PBS. Two potential mechanisms could be at work: One is that plasma proteins and ions could cause microgel deswelling, resulting in an increase in modulus. The other is that plasma proteins adsorb to the surface of the microgels, resulting in a stiffer layer of proteins that is probed by the AFM tip. To tease out the relative contributions of these two options, it is

useful to re-examine the studies by Tagit et al. and Hashmi et al. discussed above. While there exists a stark contrast in the absolute modulus measurements between the two, the *relative* increase in modulus before and after the VPTT is similar – microgels tend to increase in Young's modulus by approximately an order of magnitude after their VPTT. Since microgels exposed to plasma did not stiffen to this degree, it is unlikely that the plasma caused them to fully collapse. Furthermore, **Figure 10** demonstrates that the height of microgels swollen with water, PBS, or plasma is relatively similar. If collapse were occurring, it should be detectable by AFM height profiles, as observed in the study by Hashmi et al. (*21*). From these observations, it seems more probable that the increase in stiffness is due to the adsorption of a protein corona onto the surface of microgels.

However, there is some evidence that microgels may collapse slightly upon exposure to plasma, even if it is not enough to influence their mechanical properties as dramatically as would be expected for a full volume phase transition. While AFM measurements are appropriate for measuring the relative changes in modulus for different crosslinking and solvent conditions, the process of immobilizing microgels on glass may artificially stabilize the swollen conformation, resulting in an inaccurate VPTT. For a more accurate representation of swelling behavior, DLS is more appropriate. **Table 2** showed that while all microgels are larger at physiologic saline and temperature than at conditions designed for maximum collapse, 8% BIS microgels had a smaller swelling ratio. In other words, it was harder to collapse 8% BIS microgels to the same degree as ULC or 2% BIS microgels. This is in agreement with early studies on pNIPAM microgel swelling by Gao and Frisken (*16*). Furthermore, DLS measurements of microgels suspended in plasma were largely inconclusive – ULC and 2% BIS microgels showed the same background scattering

as plasma alone. But for 8% BIS microgels in plasma at 14 ˚C, a consistent species with R_h of 150 nm was detected. It may be that when incubated with plasma, the higher crosslink density of 8% BIS microgels prevents their complete collapse in plasma, whereas microgels of lower crosslink density collapse completely. If this is true, the ramifications for *in vivo* mechanical properties are tremendous – all microgels would likely have apparent moduli close to an order of magnitude higher than those reported here. Before claiming this, however, more research on the swelling behavior of microgels in plasma is warranted.

3.5.2 Microgel Hemorheology and Margination in Whole Blood

My hypothesis that microgels may influence the bulk viscosity of blood was motivated in part by findings that other nanoparticle systems increase blood viscosity, particularly by enhancing hemolysis and stiffening red blood cells upon exposure to nanoparticles (*122*). Additionally, my hypothesis was based on preliminary findings of apparent resistance to flow of whole blood mixed with crosslinked microgels in a microfluidic model of lung microvasculature, discussed in detail in Section 4.4. Correspondingly, I hypothesized that crosslinked microgels would enhance apparent blood viscosity at high shear rates such as those experienced in lung microvasculature. Instead, **Figure 11** shows that the bulk viscosity of blood is largely unaffected by microgels of any crosslink density, even at especially high shear. In retrospect, this result may be unsurprising. For one, microgels at their physiologic concentration of 1 mg/mL occupy a volume fraction between 0.0013 and 0.0015, as per **Table 3**. This volume fraction is miniscule compared to the volume fraction of the cellular components of blood, commonly referred to as hematocrit, which ranges from 0.39-0.54 in healthy adults (*123*).

Furthermore, if microgels were indirectly influencing blood viscosity by affecting erythrocyte morphology, stiffness, or aggregation, I would expect to see evidence of this in microscopy experiments mixing microgels with whole blood. Instead, studies of microgels mixed with labeled erythrocytes, platelets, and neutrophils showed that microgels were largely ignored by other blood components.

The finding that increasing microgel crosslinking does not lead to increased margination was unexpected. As discussed in section 3.2, the Fahraeus-Lindquist effect predicts that RBCs cluster toward the center of a blood vessel due to the lift velocity generated by the gradient of shear stress. Platelets, which are about an order of magnitude stiffer than red blood cells, do not experience this force as strongly, and instead end up trapped in the "cell free layer" near the vessel wall (*115-117*). It follows that microgels, which have tunable stiffness in the same range as red blood cells and platelets as seen in **Table 1**, should show tunable margination as well. However, **Figure 12** demonstrates that regardless of crosslink density, microgels do not reliable marginate to the walls of the microfluidic channel. There are a few potential explanations for this finding. One is that the difference in shear modulus between ULC and BIS-crosslinked microgels is simply not great enough to lead to obvious changes in margination. At a recent meeting of the World Congress of Biomechanics, Chachanidze et al. showed that red blood cells can be encouraged to marginate dramatically by fixing them with glutaraldehyde. However, normal RBCs display a Young's modulus of approximately 1 kPa, as opposed to 2-3 MPa for glutaraldehyde-fixed RBCs – a difference in modulus of over three orders of magnitude (*124*). As per **Table 1**, there is only about a 4-fold difference in modulus between ULC and 8% BIS crosslinked microgels in plasma. Another complicating factor is the size of

microgels in plasma. At approximately 1 μm in diameter, microgels are smaller than all other blood cells, including platelets. Since platelet margination in whole blood depends on platelets colliding with RBCs and being forced to the cell-free layer, it is possible that microgels are too small to be affected by these collisions, and may slip between RBCs without being pushed to the margins. Further studies on controlling microgel margination in blood vessels should incorporate larger microgel particles, as well as a wider range of moduli.

3.6 Conclusion

Understanding the mechanical properties of microgel particles is crucial to predicting their *in vivo* behavior in almost any biological application. In this chapter, I outline a robust AFM-based method for investigating the Young's, shear, and bulk moduli of pNIPAM-based microgels. To the best of my knowledge, this work also represents the first report of how microgel stiffness changes upon incubation with human blood plasma, which is most representative of their eventual *in vivo* environment. In general, pNIPAM-AAc microgels exhibit an increase in modulus when exposed to plasma, though this response is most dramatic with highly-crosslinked microgels. Surprisingly, altering microgel stiffness does not measurably affect margination of microgels in whole blood; on the contrary, it appears that pNIPAM-AAc microgels in this size and stiffness range *do not reliably marginate* to the walls of blood vessels. Furthermore, microgels at common doses for therapeutic delivery and targeting do not affect bulk blood viscosity. This information will help to inform future work on injectable microgel-based therapies.

CHAPTER 4. EVALUATION OF PNIPAM-AAC MICROGEL AGGREGATION AND PULMONARY TOXICITY

4.1 Abstract

A major obstacle to the clinical translation of microgel-based technology is short half-life in blood and uptake by immune cells. While rapid clearance may be ideal for short-term delivery in acute conditions, it presents a challenge for chronic disease treatment or long-term imaging applications. In this work, I explore the effect of increasing crosslink density on blood clearance time and biodistribution. Overall, I find that the majority microgels are cleared from blood within 12 hours, regardless of crosslink density. However, microgels of higher crosslink density tend to accumulate in the lungs for at least 24 hours, and in the kidneys for at least 72 hours. Ultralow crosslinked (ULC) microgels appear to accumulate to a lesser degree. While conducting these studies, I also observed a crosslink-dependent pulmonary toxicity in some mouse models, which motivated an investigation into the mechanism behind this toxicity. I find that crosslinked microgels form a larger and more numerous aggregates in plasma that can occlude lung microvasculature. While this does not necessarily lead to whole-lung inflammation in all animals that receive crosslinked microgels, it is possible that rare large aggregates of crosslinked microgels can catastrophically block blood vessels in the lung, resulting in an event similar to a pulmonary embolism.

4.2 Introduction

Microgels have been explored for a variety of biological applications, but their clinical use is limited by several factors. One of the most important of these is rapid clearance by the spleen or uptake by the mononuclear phagocytic system (MPS) (*1*). The initial objective for this research was to determine the effect of increasing crosslinking density on biodistribution and clearance time of pNIPAM-AAc microgels. This goal was motivated in part by studies conducted by Merkel et al. showing that an 8-fold decrease in the modulus of red blood cell (RBC)-mimicking hydrogel particles resulted in a 30-fold increase in circulation time. The softest hydrogels had an average modulus of 7.8 kPa and had an elimination half-life of 93.3 hours, as opposed the stiffest hydrogels, which had a modulus of 63.9 kPa and exhibited an elimination half-life of only 2.9 hours (*96*). In Section 3.4.1, I showed that ULC pNIPAM-AAc microgels have a Young's modulus of 2.71 kPa in water, which increases to 5.63 kPa in plasma. Since these ULC particles were softer than the hydrogel microparticles used by Merkel et al., I hypothesized that ULC microgels would circulate for longer than BIS-crosslinked microgels, perhaps long enough to enable sustained delivery of therapeutic cargo over several days.

Deformable microparticles of similar sizes to those investigated in this work have previously been shown to accumulate in the liver, spleen, and lungs, likely due to the fine microvasculature present in those organs (*125*). ULC microgels have also demonstrated the ability to squeeze through pores much smaller than their hydrodynamic diameter, an ability which decreases with crosslink density (*23*). I hypothesized that this unique deformability would allow ULC microgels to avoid accumulation in microvasculature, perhaps reducing the risk of organ damage from vascular occlusion.

Shortly after beginning biodistribution and clearance studies, it became apparent that some mice that received BIS-crosslinked microgels were experiencing significant toxicity, specifically in their lungs. Noting that the mice who received ULC microgels did not show any signs of toxicity, I generated a series of hypotheses to explain how crosslinking with BIS could lead to pulmonary toxicity. The first was that BIS-crosslinked microgels raised the apparent viscosity of blood at high shear, resulting in greater stress on the endothelium of fine blood vessels. This hypothesis was disproven in Section 3.4.4. However, I noticed in static imaging of fluorescent microgels that BIS-crosslinked microgels seemed to form more large aggregates than ULC microgels did. I therefore hypothesized that BIS-crosslinked microgels form large aggregates in plasma, which become trapped in pulmonary microcirculation, resulting in endothelial damage an inflammation. Using both *in vivo* studies in mice and *in vitro* microfluidic models of pulmonary microcirculation, I explore this hypothesis and what it means for the future of microgel-based therapies.

4.3 Materials and Methods

4.3.1 Biodistribution and Clearance Time of pNIPAM-AAc Microgels

pNIPAM-AAc microgels of varying crosslink density were labeled with VivoTag 650 (PerkinElmer) through a two-step reaction: first, microgels were aminated with Tris(2-aminoethyl)amine (Sigma Aldrich) by standard EDC/Sulfo-NHS chemistry. Next, aminated microgels were incubated with Vivotag in a sodium bicarbonate buffer. Unbound dye was removed by dialysis against deionized water with a 1000 kDa dialysis membrane (Spectrum Labs). Labeled microgels were then lyophilized in 10 mg batches.

10 mg of labeled microgels were reconstituted in 0.5 mL of sterile saline for a final concentration of 20 mg/mL. 50 μL was injected into 8 week old C57BL/6 mice (Jackson Laboratory) via tail vein injection, for a total dose of 1 mg per 20 g mouse (50 mg/kg). Mice were left for 5 minutes to allow microgels to circulate in the bloodstream. After 5 minutes, 20 μL of blood was drawn from the tail vein, and pipetted into heparinized tubes. The same process was repeated at 30 minutes, and 1, 2, 6, 12, 24, 30, 36, and 48 hours. Blood was diluted with 80 μL PBS and pipetted into a black 96-well plate, where it was scanned on a near-IR scanner (LICOR). Fluorescent signal was compared against a standard curve of microgels diluted in PBS to calculate concentration of microgels in blood at each time point. To mimic the potential degradation of the fluorescent signal *in vivo*, the standard curve plate was stored in a 37 ˚C incubator and read each day to generate a new standard curve.

Following sacrifice via terminal overdose of ketamine/xylene or CO_2 inhalation, mice were dissected and heart, kidneys, lungs, spleen, and liver were harvested. Organs were scanned on the near-IR LICOR scanner to assess fluorescent signal.

4.3.2 Histology and IHC of Lung Sections

For studies specifically investigating pulmonary toxicity of microgels, unlabeled microgels were used. 100 uL of a 10 mg/mL microgel suspension was injected into 8 week old male C57BL/6 mice (Jackson Laboratory, ME) via tail vein injection, for a total dose of 1 mg per 20 g mouse (50 mg/kg). Following injection, mice were monitored for signs of discomfort or pain until their terminal endpoint at 24 or 48 hours. Four mice were included per condition and timepoint. After their endpoint, mice were sacrificed by either

CO_2 inhalation or overdose of ketamine/xylene, depending on the experiments performed after sacrifice.

Following sacrifice, mice were dissected and lungs were harvested. Organs were fixed in 4% paraformaldehyde overnight. Portions of each organ were saturated with sucrose prior to embedding with OCT in preparation for cryosectioning, or saturated with 70% ethanol prior to embedding with paraffin. Tissue sections were generated, and selected sections were stained with hematoxylin and eosin (H&E) or Martius Scarlet Blue (MSB) stain for fibrin deposition.

For immunohistochemical analysis of inflammatory markers, paraffin sections were deparaffinized, quenched in methanol and hydrogen peroxide, antigen retrieved in citrate, and stained with primary antibodies for F4/80 for macrophages (BD Biosciences cat# 746070), Ly-6G for neutrophils (BioLegend cat# 127601), and VCAM-1 (Abcam cat# ab134047) and ICAM-1 (ThermoFisher cat# MA5407) on endothelial cells. Secondary signal was amplified with an avidin-biotin complex prior to detection with 3,3'-diaminobenzidine (DAB, Abcam).

4.3.3 Flow Cytometry

Portions of lung tissue were digested in collagenase, then pushed through a fine mesh to break up the tissue. Red blood cells were lysed, and remaining cellular components were labeled with antibodies toward F4/80 (BD Biosciences cat# 746070) and Ly-6G (BioLegend cat# 127601) for macrophages and neutrophils, respectively, prior to analysis by flow cytometry at the University of Virginia flow cytometry core facility. Cell

infiltration was quantified by the percentage of CD45+ cells that stained positive each marker.

4.3.4 Cytokine Quantification

Following sacrifice via terminal overdose, approximately 1 mL of blood was drawn from mice via cardiac puncture, into heparinized tubes. Plasma was isolated via centrifugation. Bronchoalveolar lavage fluid (BALF) was obtained by flushing the lungs with 3 mL of saline with protease inhibitor. Cytokine quantification was performed via the Luminex mouse "megaplex" assay (ThermoFisher, MA), which measures 32 distinct secreted cytokines, listed in **Table 4**.

Table 4: List of cytokines analyzed by the Luminex mouse "megaplex" assay.

IL-1α	IL-1β	IL-2	IL-3	IL-4	IL-5	IL-6	IL-7
IL-8	IL-9	IL-10	IL-12p40	IL-12p70	IL-13	IL-15	IL-17A
CC-11	G-CSF	GM-CSF	IFN-γ	IP-10	KC/GRO	LIF	MCP-1
M-CSF	CXCL-9	MIP-1α	MIP-1β	MIP-2	CCL-5	TNFα	VEGF

4.3.5 Analysis of Static Microgel Aggregate Formation

To assess the size of microgels formed in varying solvents, lyophilized Cy3b-labeled or unlabeled microgels were resuspended in different solvents at a concentration of 1 mg/mL and left to incubate for 1 hour on a rotisserie mixer at 25 ˚C. 10 uL of the suspension was spotted onto a coverslip blocked with bovine serum albumin to prevent adhesion to the substrate, and imaged with confocal microscopy. Labeled microgels were imaged with fluorescence and unlabeled microgels were imaged with differential

interference contrast. Size was calculated with the object finding tool of Volocity image analysis software (PerkinElmer).

4.3.6 In Vitro *Microfluidic Models of Lung Microvasculature Occlusion*

The fabrication of a polydimethylsiloxane microfluidic to mimic microvasculature has been discussed in previous work by the Lam group (*126*). Briefly, the device consists of branching microfluidic channels, the smallest of which are 6 μm wide x 15 μm tall. A schematic of several of the microchannels in the device is shown in **Figure 13**.

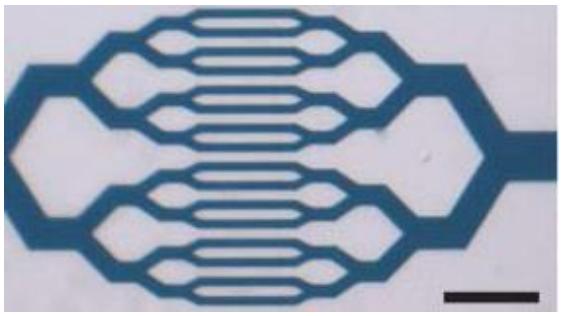

Figure 13: Schematic of pulmonary microvasculature microfluidic device. Scale bar 100 μm. Adapted from Rosenbluth et al. (*126*)

Cy3b-labeled microgels of varying crosslink density were mixed with citrated whole blood or plasma and perfused at a wall shear stress of 150 dyne/cm^2 to recapitulate physiologic shear in microvasculature (*105*). In certain experiments, platelets were labeled to visualize potential clot formation. In others, microgels were suspended in plasma instead of whole blood. The microfluidic device was imaged with confocal videomicroscopy, and occlusion of the channels over time was determined by manual review of the videos.

4.3.7 In vitro *Microfluidic Model of Endothelial Damage*

Branching or straight channel microfluidic devices were coated with endothelial cells as described in previous work by the Lam group (*127*). Briefly, devices were coated with collagen and fibronectin, then human umbilical vein endothelial cells were perfused through the device and cultured for two to three days until confluent. Microgels were mixed with either media or whole blood and perfused at physiologic shear through the device. In certain experiments, the device was pretreated with microgels for 5 hours prior to imaging. In others, labeled microgels were mixed with whole blood directly before perfusing and imaging. Endothelial damage was assessed by disruption of the endothelial cell layer and staining of VCAM-1.

4.4 Results

4.4.1 Biodistribution and Clearance Time of pNIPAM-AAc Microgels

Early attempts at determining the clearance time of pNIPAM-AAc microgels of varying crosslink density indicated that microgels injected into mice at a dose of 50 mg/kg reached a peak blood concentration of approximately 1.5 mg/mL a few minutes after injection, and displayed a half-life of about 12 hours. There was no apparent difference between crosslinking conditions, though this preliminary study was plagued by low sample number and problems with determining a robust standard curve. Once the process was streamlined and the study was properly powered, it became apparent that the clearance time of microgels in blood was much faster than previously thought. **Figure 14** shows that the microgel signal decays rapidly, with a half-life of only 2-3 hours, and becomes undetectable in blood after 30 hours.

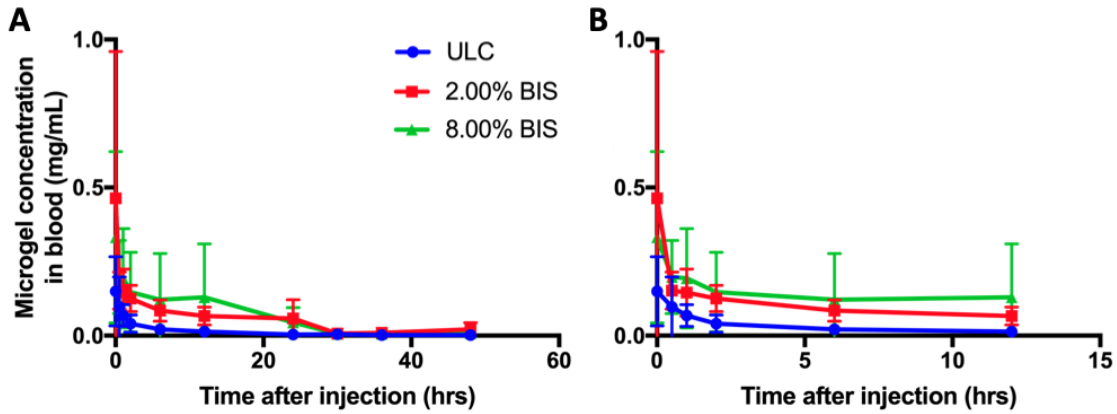

Figure 14: Blood clearance time of microgels of varying crosslink density injected into mice at 50 mg/kg. **A,** full 48 hour time course. **B,** magnified view of first 12 hours, showing rapid clearance in the first few hours.

72 hours after injection, mice were sacrificed and heart, lungs, kidneys, spleen, and liver were scanned to check for signal from the microgels. **Figure 15** shows a representative scan for each microgel crosslinking density. Overall, the microgel signal was very low at 72 hours, except in the kidneys, where microgels seem to accumulate. ULC microgels appeared to accumulate less than crosslinked microgels, which also were detectable at a low level in the lungs.

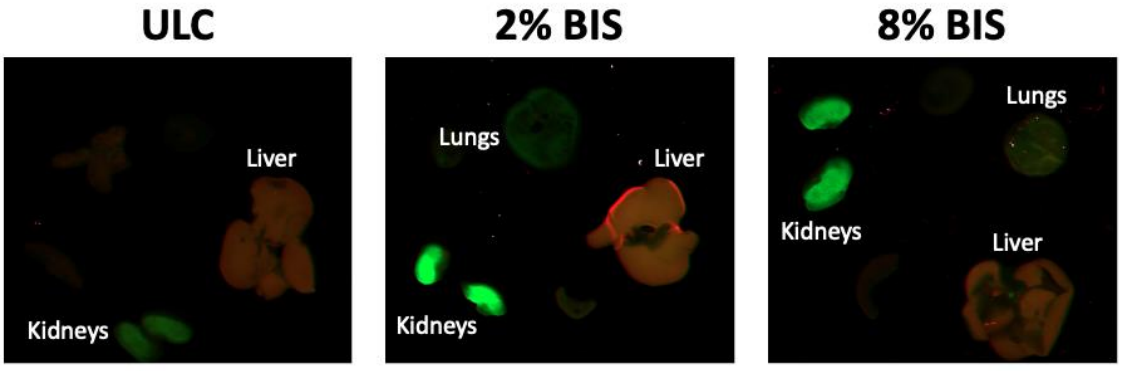

Figure 15: 72 hour scans of organs dissected from mice injected with 50 mg/kg labeled microgels of varying crosslink density. Green is the microgel signal, and red is background fluorescence showing the outline of the liver. Heart and spleen were also imaged, but fluorescent signal was undetectable.

Notably, two mice from this study died prior to their terminal endpoint at 72 hours. One, who received 2% BIS-crosslinked microgels, died at some point between 12 and 24 hours. The second received 8% BIS-crosslinked microgels and died at around 30 hours. In both cases, the mice had appeared lethargic and struggling to breathe. These mice were dissected, and their organ scans are shown in **Figure 16**.

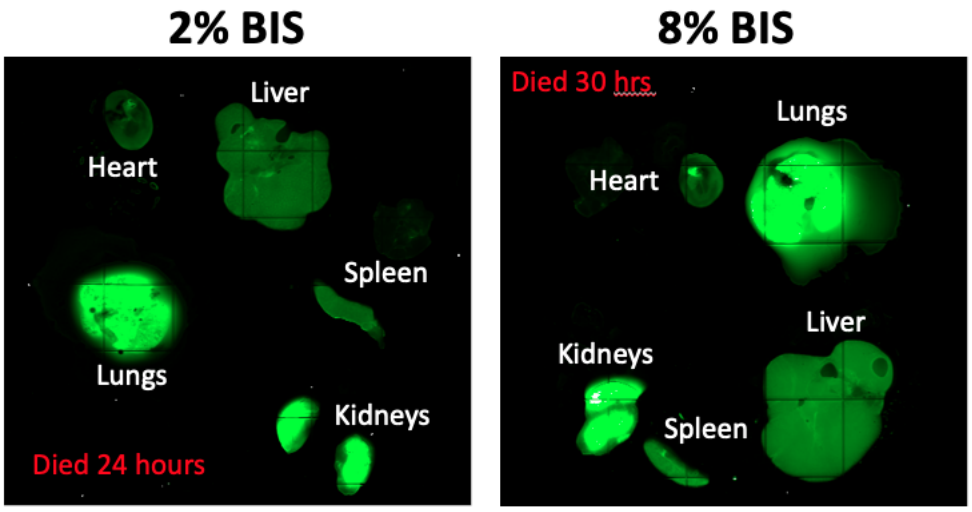

Figure 16: Organ scans of mice that died before their terminal endpoint at 72 hours.

The microgel signal in all organs is higher than the signal at 72 hours, which is expected at an earlier timepoint. Kidneys still show a comparatively higher signal than other organs, but the most striking difference is the bright signal from the lungs not seen at 72 hours. Taken together with the signs of breathing problems, this data motivated the hypothesis that crosslinked microgels may induce pulmonary toxicity to a greater degree than ULC microgels. The remaining data in this chapter is focused on exploring this hypothesis.

4.4.2 Effects of Microgels on Lung Morphology and Histology

Crosslinked microgels were found to have a greater influence than ULC microgels on the gross morphology of lungs dissected from mice at 24 and 48 hours post injection (**Figure 17**). Mice that received ULC microgels had large, nearly white lungs with clearly defined lobes, similar to mice that received a saline control. By contrast, mice that received 2% BIS- or 8% BIS-crosslinked microgels showed macroscopic signs of lung damage, including darkened lung tissue, compressed structure, and bleeding. These visual differences were apparent at 24 hours, and persisted through the 48 hour time point.

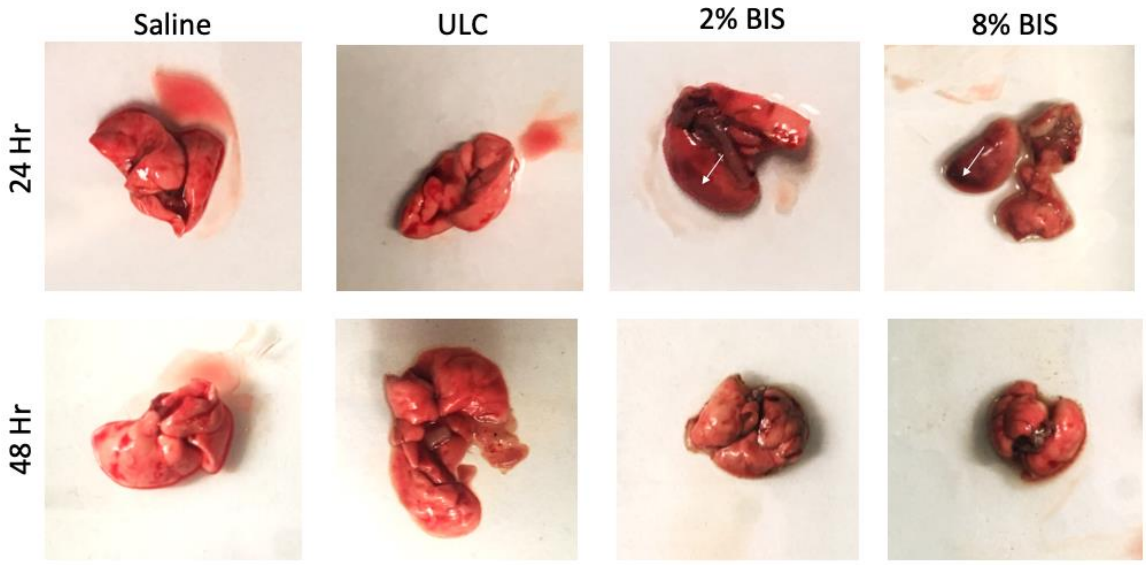

Figure 17: Macroscopic images of mouse lungs dissected 24 or 48 hours after receiving the indicated treatment. White arrows indicate regions of darkened lung tissue, suggesting inflammation or tissue damage.

In order to investigate the microscopic changes in lung tissue as a result of microgel exposure, lung sections were generated and stained with H&E (**Figure 18**). At 24 hours, lung structure from mice that received ULC microgels resembled that of the saline control, whereas mice that received 2% BIS- or 8% BIS-crosslinked microgels showed a slightly denser alveolar structure. This effect was more pronounced at 48 hours, especially in the lungs of mice who received 8% BIS-crosslinked microgels.

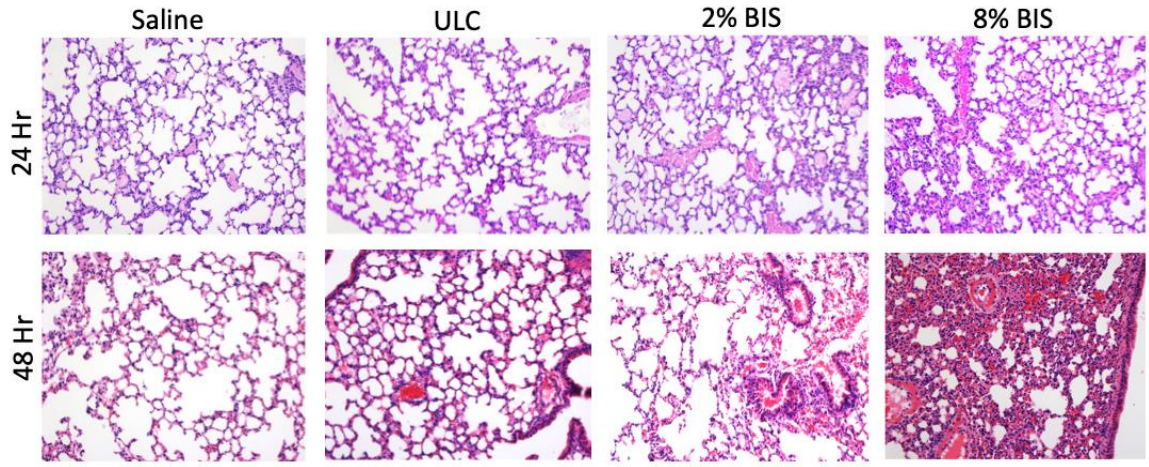

Figure 18: H&E staining of mouse lung sections 24 or 48 hours post injection with microgels of varying crosslink density. 20X magnification.

Since H&E staining suggested that lung tissue was inflamed upon exposure to crosslinked microgels, IHC was also performed on lung sections to assay cell infiltration and inflammatory response. Staining for macrophages via the F4/80 receptor (**Figure 19**) showed little to no dependence on crosslinking density – even the saline control showed positive staining for macrophages, which may suggest resident macrophages in the lung.

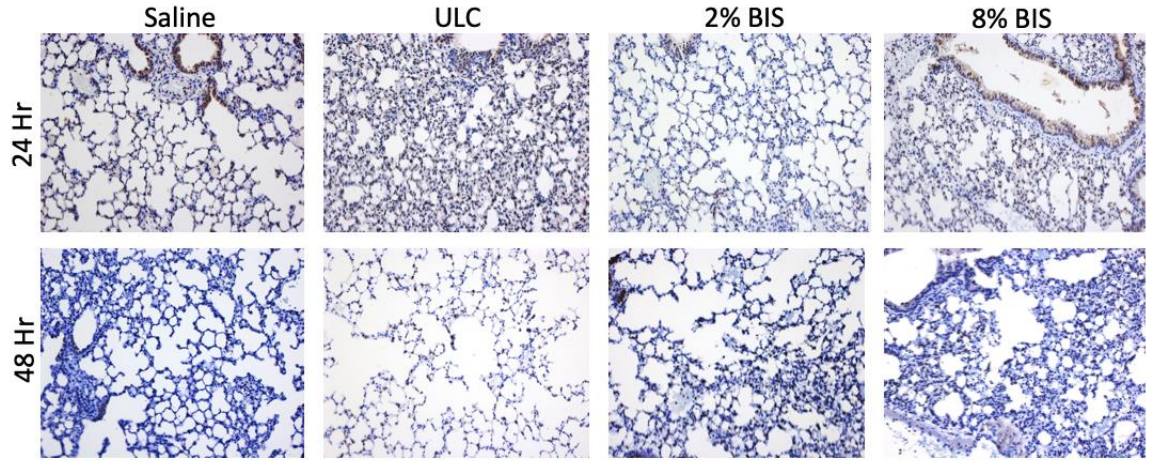

Figure 19: F4/80 IHC for macrophages on mouse lung sections 24 or 48 hours post injection with microgels of varying crosslink density. 20X magnification.

Staining for neutrophils via Ly-6G also showed minimal neutrophil infiltration, though certain areas of lung sections from mice treated with 8% BIS-crosslinked microgels did stain positive for neutrophils (**Figure 20**).

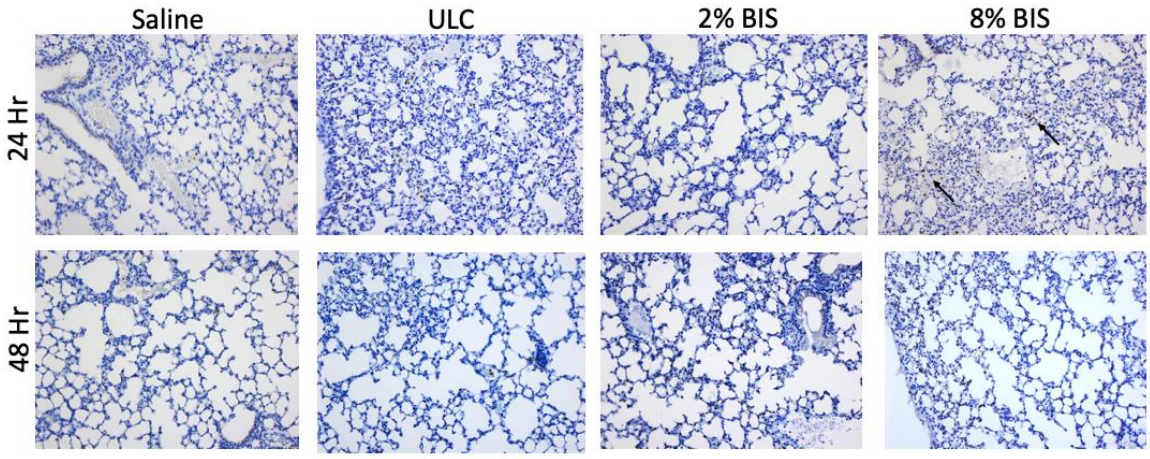

Figure 20: Ly-6G IHC for neutrophils on mouse lung sections 24 or 48 hours post injection with microgels of varying crosslink density. 20X magnification. Arrows show positive staining for neutrophils.

Since cellular signs of inflammation were largely absent, sections were next stained for VCAM-1, a marker of endothelial damage. **Figure 21** shows that VCAM-1 expression in lung endothelium is greatly enhanced in sections from lungs exposed to crosslinked microgels, and less enhanced in sections from lungs that were exposed to ULC microgels.

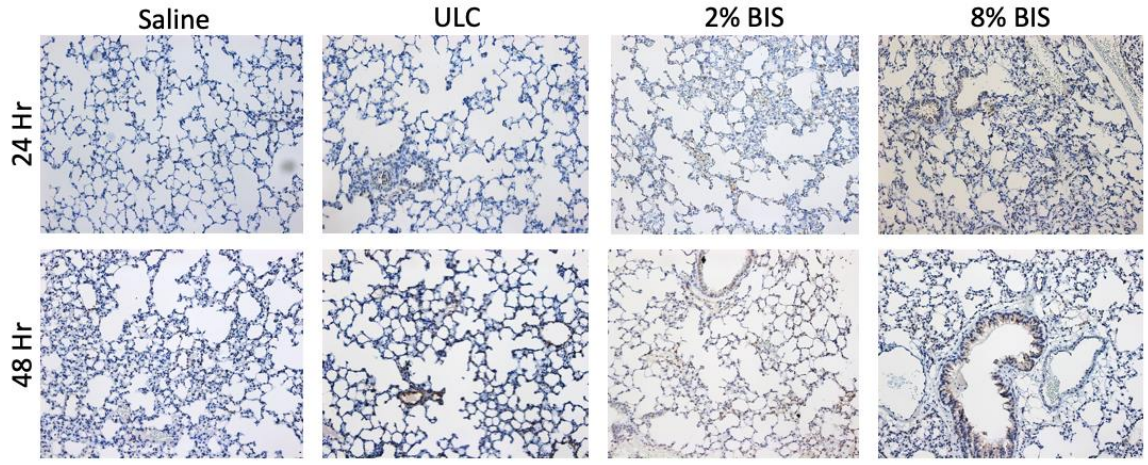

Figure 21: IHC staining for VCAM-1 on mouse lung sections 24 or 48 hours post injection with microgels of varying crosslink density. 20X magnification.

4.4.3 Inflammatory Response of Lung Tissue Exposed to Microgels

Since injection of BIS-crosslinked microgels appears to result in denser lung tissue and expression of VCAM-1, I hypothesized that they may induce an inflammatory response in the lung. To test this hypothesis, flow cytometry was performed on homogenized lung tissue as well as bronchoalveolar lavage fluid (BALF) to check for infiltration of macrophages and neutrophils. **Figure 22** shows that regardless of time point of microgel condition, the amount of macrophages and neutrophils in lung tissue and BALF was not significantly different than the saline control. This is perhaps unsurprising, as **Figures 19** and **20** showed minimal staining of these cells in lung sections as well. However, it is interesting to note that the 48 hour, 8% BIS condition has an exceptionally high error bar. This is due to one mouse in this condition showing consistently high levels of neutrophils and macrophages. While the overall trend is not significant, this finding perhaps points to the relative rarity of catastrophic toxic events from microgels.

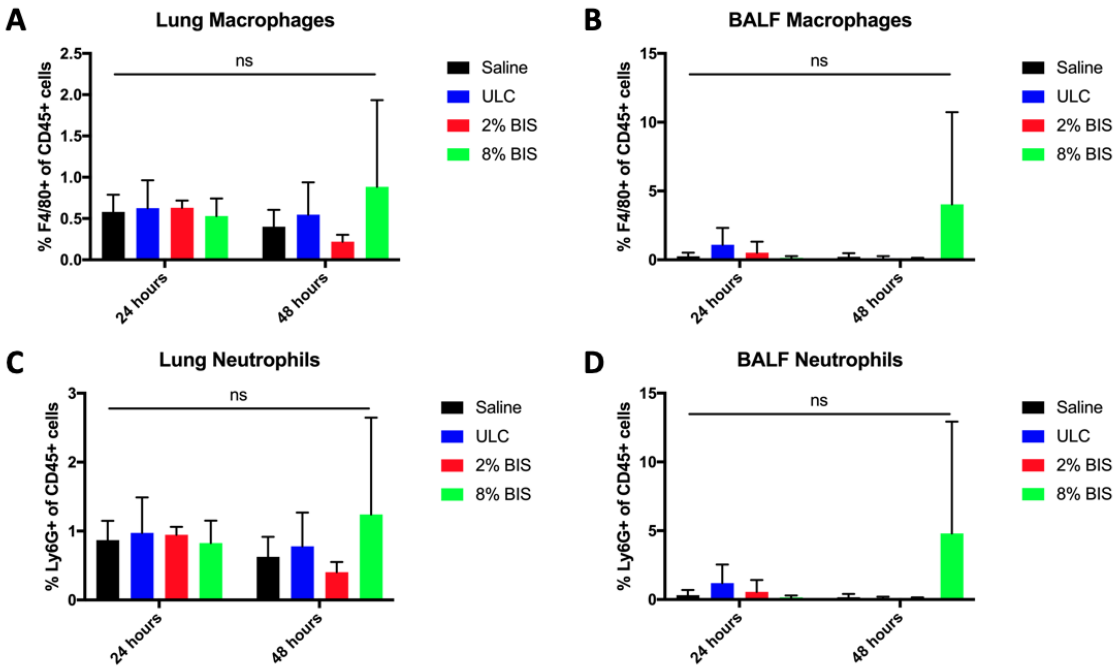

Figure 22: Flow cytometry for macrophages (F4/80, **A** and **B**) and neutrophils (Ly6G, **C** and **D**) in partially homogenized lung tissue (**A** and **C**) and BALF (**B** and **D**). Significance determined by ANOVA with Tukey's post-test, n = 4.

Next, plasma and BALF were analyzed for levels of cytokines associated with endothelial damage and inflammation, namely IL-1α, IL-1β, TNFα, and IFNγ. **Figure 23** shows that for the most part, there was no significant association between microgel treatment and inflammatory cytokine level. **Figure 23B** indicates that plasma IL-1β may be elevated in mice that received 2% BIS-crosslinked microgels at 24 hours, but the trend does not hold with mice that received 8% BIS-crosslinked microgels. Another interesting note is the high mean value and variability of plasma IFNγ in mice that received 8% BIS-crosslinked microgels for 48 hours (**Figure 23D**). This was the same mouse that showed increased infiltration of neutrophils and macrophages in **Figure 22B** and **D**.

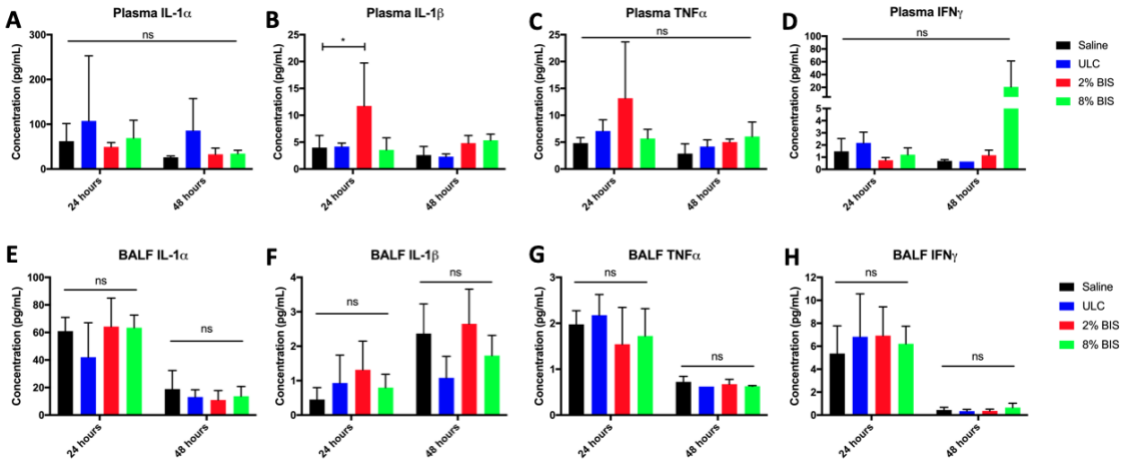

Figure 23: Inflammatory cytokines in plasma (**A-D**) and BALF (**E-H**) of mice injected with microgels of varying crosslink density. Significance determined by ANOVA with Tukey's post-test, n = 4.

4.4.4 Formation of Crosslink-dependent Microgel Aggregates

Figure 24 shows the size of microgel aggregates that spontaneously form upon resuspension in various solvents. Since there was a wide range of aggregate sizes in each condition, the data is presented in two ways: first, a frequency distribution of small aggregate sizes (< 10 μm^2) is shown, which captures the vast majority of aggregates present. Next, the full set of data for each condition is shown on a logarithmic scale, to visualize the rare large aggregates that form in each condition.

In complete plasma, ULC microgels form the smallest aggregates, with a peak at approximately 0.5 μm^2. 2% BIS-crosslinked microgels are slightly larger with a peak at ~1.5 μm^2. 8% BIS-crosslinked microgels have a wider distribution of small aggregate sizes, with many microgel aggregates ranging in size from 2 to 4 μm^2. When the data is presented as a whole, it is also apparent that BIS-crosslinked microgels form some aggregates that are greater than 1000 μm^2, whereas the largest ULC microgel aggregate is about 200 μm^2.

Since plasma is a complex fluid, it is worth considering which components contribute to this disparity in aggregate formation. Incubation with physiologic concentration of albumin alone results in a greater proportion of large (> 100 μm^2) aggregates across all conditions, though BIS-crosslinked microgels still form more of these than ULC microgels. Exposing microgels to only immunoglobulin results in a distribution similar to whole plasma, where BIS-crosslinked microgels clearly form larger aggregates than ULC microgels. When protein is taken out of consideration entirely, and microgels are resuspended in only PBS, the effect reverses – all microgels form smaller aggregates without protein, but BIS-crosslinked microgels actually form even *smaller* aggregates than ULC microgels, with few aggregates over 10 μm^2. Curiously, in deionized water alone, BIS-crosslinked microgels once again form a greater proportion of large aggregates than ULC microgels.

To address concerns that aggregation was an artefact of microgel labeling, some experiments were repeated with unlabeled microgels and differential interference contrast imaging, which showed similar trends, but slightly smaller maximum aggregate size.

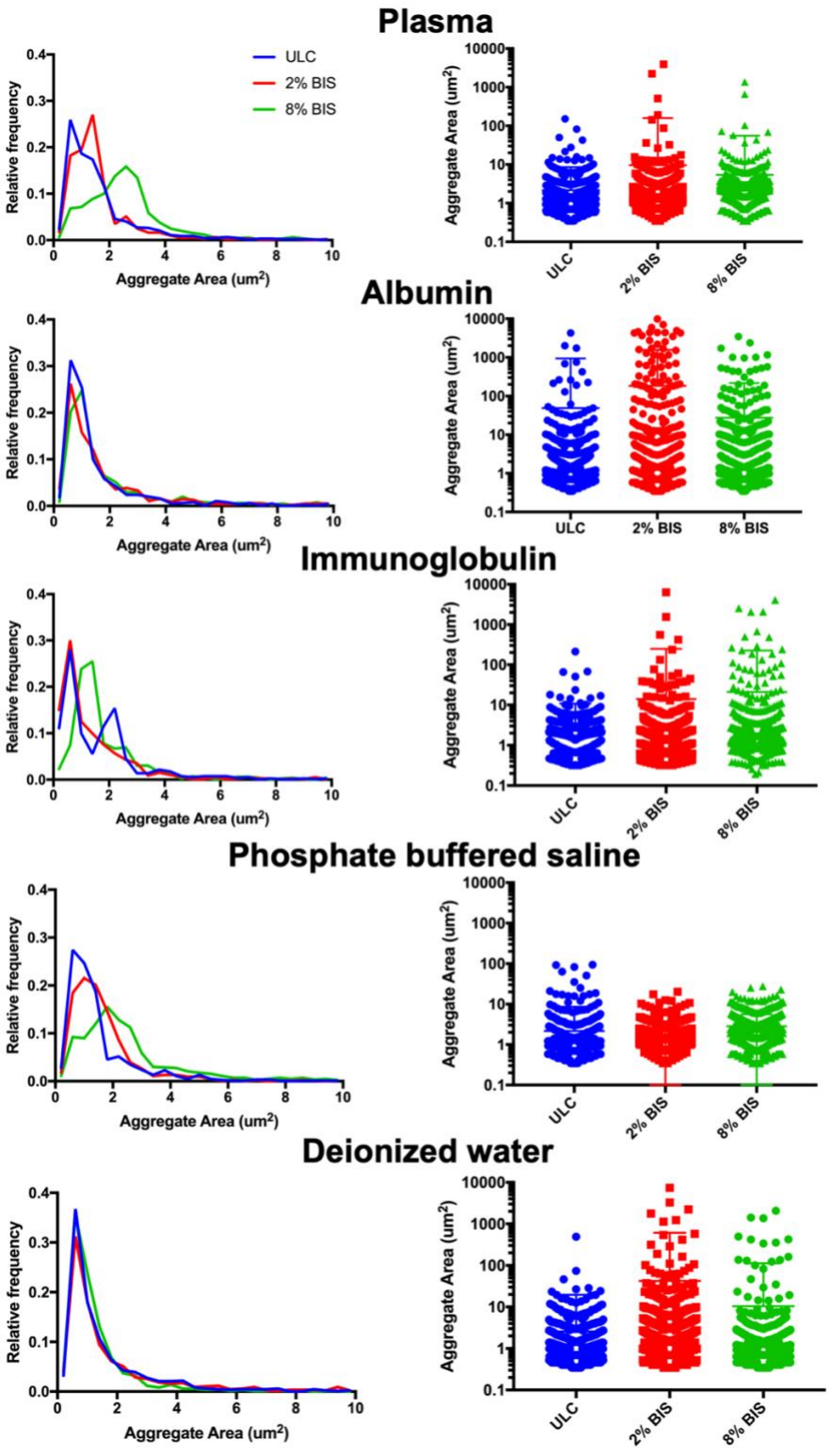

Figure 24: Formation of microgel aggregates in various solvents. The left column shows a frequency distribution of small (< 10 μm^2) aggregates, whereas the right column shows the full set of data on a logarithmic scale. N > 750 for each condition.

4.4.5 Mass Spectrometry Analysis of pNIPAM-AAc Microgel Protein Corona

To test the hypothesis that differences in microgel aggregation arise from differential protein binding, the protein corona of microgels of varying crosslink density was analysed using protein mass spectrometry after incubation with human plasma. **Figure 25** shows the breakdown of serum proteins bound to each microgel. Unsurprisingly, the most abundant protein in the corona was serum albumin, which comprised from 34-40% of the entire protein corona of the microgels. This result corroborates work by Miceli et al. (*49*). Immunoglobulin heavy chains were the next most abundant, followed by TNF-α. Microgels crosslinked with 2% BIS showed a slightly higher proportion of albumin in their protein corona, but this trend did not hold with increasing crosslinking. This suggests that overall, it is unlikely that microgel crosslink density significantly influences the composition of the protein corona.

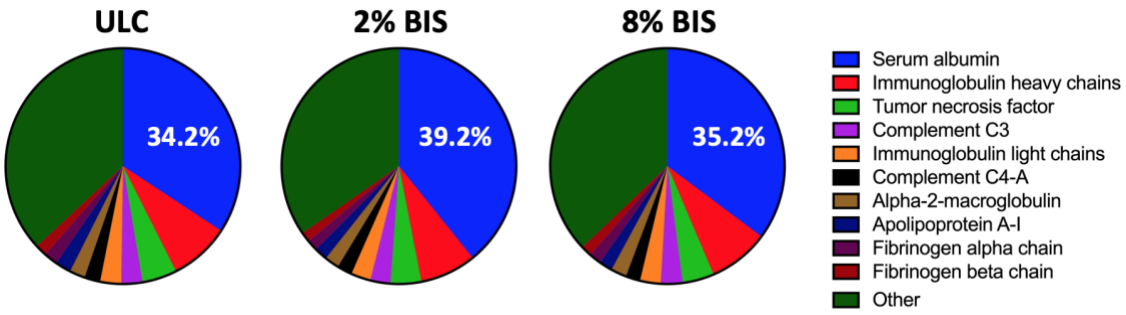

Figure 25: Proportion of serum proteins bound in the protein corona of microgels of varying crosslink density.

4.4.6 pNIPAM-AAc Microgel Aggregates Can Occlude Lung Microvasculature

Having established that pNIPAM-AAc microgels form large aggregates in a crosslink-dependent manner in plasma, the next goal was to test whether these aggregates were large and durable enough to occlude lung microvasculature. A branching microfluidic

device consisting of channels as small as 6 μm wide by 15 μm tall was used to model pulmonary microcirculation. **Figure 26A-B** shows that at a physiologic shear of 150 dyne/cm^2, microgel aggregates in human plasma become trapped in the small channels of the device. As expected, BIS-crosslinked microgels show more and larger aggregates that occlude the channels.

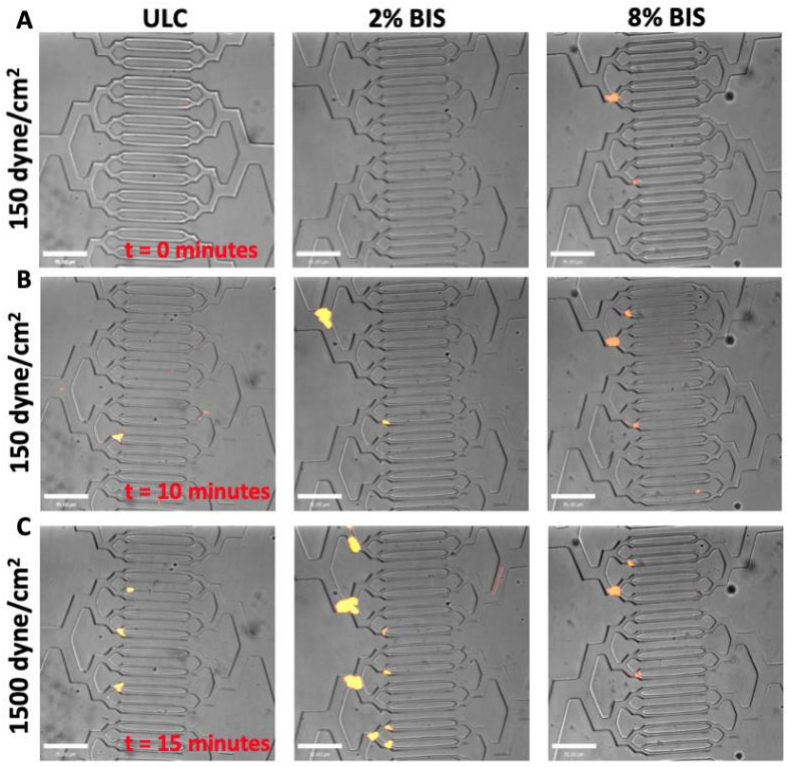

Figure 26: Microgels in human plasma form aggregates large and durable enough to occlude a microfluidic model of lung microvasculature. Microgels shown in orange/yellow. **A,** devices at the start of the run. **B,** devices after 10 minutes of plasma/microgel mixture at physiologic shear (150 dyne/cm^2). **C,** devices after an additional 5 minutes of 10X physiologic shear. Scale bar, 70 μm.

After 10 minutes of flow at physiologic shear, the flow rate was increased by 10-fold to test whether the enhanced pressure could dislodge microgel aggregates and force them through the channels. Although a few small aggregates were moved through the channels at this higher flow rate, most aggregates remained lodged at the inlet of the small

channels (**Figure 26C**). This demonstrates that although ULC microgels are less likely to form large aggregates than BIS-crosslinked microgels, all pNIPAM-AAc microgels have the potential to form aggregates large and durable enough to occlude lung microvasculature.

This experiment was also performed mixing microgels with whole blood and perfusing through the device at physiologic shear, then measuring occlusion by manually recording the channels that stopped flowing blood at specific time points. These results are difficult to interpret, as even control blood will occlude small microfluidic channels over time due to non-specific clotting or aggregates of red blood cells that become lodged in the channels. Even so, **Figure 27** shows that while there is high variability between runs, BIS-crosslinked microgels result in a higher percentage of channels occluded by the end of a 10 minute run.

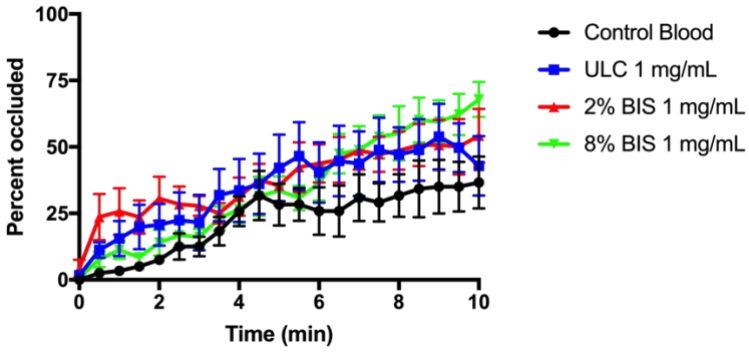

Figure 27: Occlusion of microfluidic channels with whole blood mixed with microgels of varying crosslink density. Data is presented as mean ± standard error, n = 6.

4.4.7 Effect of Microgel Perfusion on Endothelialized Microfluidic

To investigate the link between microgel aggregates and endothelial damage, microgels were mixed in endothelial cell growth media and perfused through an

endothelialized microfluidic device. Perfusion with whole blood was precluded by clotting upstream of the device, resulting in uneven flow and filtering of microgel aggregates. Damage to endothelium was determined by absence of endothelial cells along the channel, as well as enhanced VCAM-1 expression on endothelial cells. **Figure 28** shows that regardless of microgel treatment, the endothelial cell layer remained confluent and VCAM-1 expression was similar between all conditions. However, this may be due to the comparatively large size of the channels in relation to the previous microfluidic. Since smaller channels cannot be endothelialized, these channels were 100 μm^2 tall by 100 μm^2 wide.

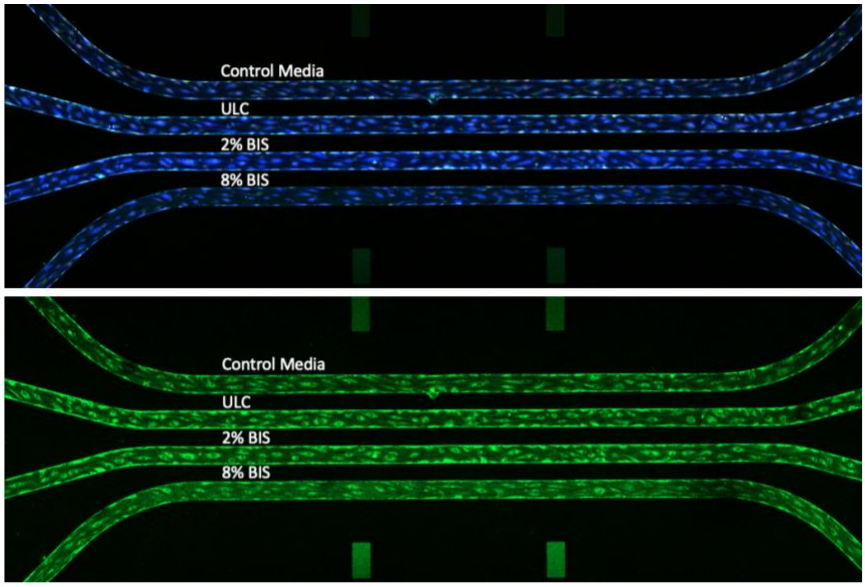

Figure 28: Endothelialized cell device after 5 hours perfusion of growth media plus microgels of varying crosslink density. Top, full fluorescent signal with endothelial cell nuclei in blue, VCAM-1 in green. Bottom, brightened version of VCAM-1 signal. Channels measure 100 μm^2 tall by 100 μm^2 wide.

4.5 Discussion

4.5.1 Crosslink-dependent pNIPAM-AAc Microgel Aggregate Formation

Microgel aggregate formation is a complex process with multiple influencing factors. In whole plasma, all microgels form aggregates, but 8% BIS-crosslinked microgels form a broader distribution of "small" aggregates (< 10 μm^2) than ULC or 2% BIS-crosslinked aggregates. Both varieties of BIS-crosslinked microgels form a small number of massive aggregates in excess of 1000 μm^2, whereas all ULC aggregates were smaller than 200 μm^2. To put this data in the context of pulmonary microcirculation, it is useful to note that the average capillary diameter in the human lung is 6.3 μm, corresponding to a cross sectional area of about 31 μm^2 (*128*). Thus, any aggregate in excess of this size has the potential to occlude lung microvasculature. When suspended in PBS alone, without protein and other biomolecules, the small aggregate trend remained the same, but few very large aggregates were formed. In fact, ULC microgels seemed to form more large aggregates, up to ~ 100 μm^2, than BIS-crosslinked microgels. To ascertain which plasma components could be responsible for enhanced, crosslink-specific aggregation, microgels were suspended in either albumin or immunoglobulin alone, each at their approximate physiologic concentration. Albumin resulted in large aggregate formation across all microgel varieties, though BIS-crosslinked microgels still a greater number of aggregates greater than 1000 μm^2. Immunoglobulin resulted in a similar profile to whole plasma, where BIS-crosslinked microgels formed larger aggregates than ULC microgels. Notably, 8% BIS microgels suspended in immunoglobulin formed even more larger aggregates than 8% BIS microgels in plasma. These results agree with previous work by Müller et al.

showing that albumin and immunoglobulins in the protein corona contribute to nanoparticle aggregation in plasma (*39*). Interestingly, microgels in deionized water also show a similar aggregation profile to those in whole plasma.

How does it make sense that PBS is the only condition without large aggregate formation? A potential explanation is that aggregates can result from multiple distinct forces. Looking first at the two conditions without protein, it is apparent that in deionized water, all microgels form small aggregates ($< 10\ \mu m^2$) that are approximately the same size, whereas in PBS, BIS-crosslinked microgels form small aggregates with a broader distribution of sizes. This suggests that there is either an electrostatic component stabilizing small microgel aggregates in water that is shielded when microgels are suspended in PBS, or that microgel deswelling in PBS promotes aggregation. Section 3.4.3 demonstrated that the swelling behavior of the microgels is very similar, regardless of crosslink density, so it is unlikely that differences in swelling are behind this response. Since all microgels carry a net negative charge due to AAc, it is possible that the electrostatic explanation is valid for small aggregate sizes. The particularly large aggregates in deionized water may be due to hydrophobic interactions between the dye conjugated to microgels, though it is unclear why BIS-crosslinked microgels still form more large aggregates. When protein is introduced, it is clear that albumin promotes aggregation to a greater extent than immunoglobulin. From that perspective, it is possible that BIS-crosslinked microgels bind a greater proportion of albumin that do ULC microgels.

Miceli et al. found slightly different results regarding pNIPAM-based microgel protein binding an aggregate formation, though the microgels in that study were copolymerized with dendritic polyglycerol (dPG). Their results point to immunoglobulin

binding as a source of reversible aggregation of microgels, and note that immunoglobulin bound to a greater extent when the microgels were partially collapsed at physiologic temperature (*49*). This perhaps suggests that the most important source of microgel aggregation is hydrophobic protein binding. From this perspective, it is possible that BIS-crosslinked microgels are more hydrophobic than ULC microgels regardless of swelling state, making them more prone to aggregation.

It should be noted that all of the data shown for static microgel aggregate formation were from microgels that had been pre-labeled with a Cy3b-NHS ester dye. The labeling procedure is two-step: first, the AAc sites on microgels were aminated with Tris(2-aminoethyl)amine, followed by incubation with Cy3b-NHS ester. In the process, most of the net negative charge of the microgels was likely lost. This could have the effect of lowering the VPTT of the microgels, making them more likely to collapse into their hydrophobic states, perhaps promoting aggregation. To address this concern, some studies were performed with unlabeled microgels, using differential interference contrast imaging. Although the maximum aggregate size was smaller in these studies, there was still evidence that crosslinked microgels aggregated to a greater size than ULC microgels.

4.5.2 Interpretation of Biodistribution and Clearance Time

The blood clearance time of pNIPAM-AAc microgels was shown to be much more rapid than originally thought. Most of the microgel signal in blood had decayed by 12 hours, and it was undetectable after 30 hours. Initially, I hypothesized that ULC microgels, by virtue of their lower elastic modulus, would stay in circulation for longer than BIS-crosslinked microgels, following work by Merkel et al. (*96*). However, there are several

key differences between RBC-mimicking particles in the Merkel study and the pNIPAM-AAc microgels explored here. For one, the hydrogels in the Merkel study were designed to be discs with 5.2-5.9 μm diameters and 1.22-1.54 μm tall, recapitulating the shape of native RBCs. Not only do large particles stay in circulation for longer than smaller ones, but non-spherical particles are known to have a longer circulation time than spherical ones (*95*). Since the pNIPAM-AAc microgels investigated here are approximately 1 μm in diameter, and universally spherical, it stands to reason that their circulation time would be much shorter, and any differences between crosslinking conditions would be negligible. Furthermore, the difference in modulus between the stiffest and softest particles in Merkel's study was about 8-fold, as opposed to an approximate 4-fold difference between ULC and 8% BIS-crosslinked microgels.

Although the particles did not last long in blood, there was evidence of a high microgel signal in lungs and kidneys at 24 hours, with signal remaining in the kidneys for up to 72 hours. Considering the size of the microgel aggregates discussed in Section 4.5.1, a more apt comparison for biodistribution may be a study of purposely aggregated PEG microgels with an average aggregate diameter of 30 μm. Deshmukh and colleagues found that these aggregates accumulated in the lung within 30 minutes, and persisted for 48 hours before being enzymatically degraded to their principal components and eliminated by renal filtration (*106*). Putting these results in the context of the findings presented here, a two phase model of pNIPAM-AAc microgel biodistribution can be considered: first, individual microgels are rapidly cleared within 12-24 hours. Next, microgel aggregates accumulate in the lungs and kidneys, until they are degraded over the course of 3 to 4 days.

4.5.3 Pulmonary Toxicity of pNIPAM-AAc Microgel Aggregates

The microfluidic experiments demonstrate that microgel aggregates are large and durable enough to occlude lung microvasculature, even at supraphysiologic flow rates. As with static experiments, BIS-crosslinked microgels formed more large aggregates that became trapped in the microchannels. While there was little evidence of endothelial damage in the endothelialized microfluidic device, there are a few potential explanations for this. For one, the channels of the endothelialized device were much larger than the device used to model pulmonary microvasculature. Whereas the pulmonary device had a smallest channel size of 6 μm wide by 15 μm tall (90 μm^2 cross-sectional area), the endothelialized device had a channel size of 100 μm wide by 100 μm wall (10,000 μm^2 cross-sectional area). **Figure 24** demonstrates that even in BIS-crosslinked conditions, no aggregates approached this size, so it's possible that no aggregates made contact with the endothelial wall. Furthermore, since upstream clotting prevented running these experiments in whole blood, most microgels were probably pushed away from the endothelialized walls of the channel by lift velocity from the shear gradient, known as the Fahraeus-Lindquist effect (*115*).

While discrete instances of toxicity were observed *in vivo*, the overall inflammatory response of microgels was not greater than that of saline controls. This is perhaps unsurprising; Miceli et al. found that pNIPAM-based microgels form a dysopsonin-rich protein corona, which would reduce their likelihood of being recognized and phagocytosed by immune cells such as macrophages and neutrophils (*49*).

Instead, an alternate explanation for toxicity emerges. Instead of BIS-crosslinked microgel aggregates causing incremental damage to pulmonary endothelium, the instances of toxicity could be explained by the rare, truly massive microgel aggregates that form from BIS-crosslinked microgels. Instead of inflammation, toxicity like this could be more akin to a single catastrophic event such as a pulmonary embolism. It may not happen in every mouse (or human) injected with BIS-crosslinked microgels, but the risk for an especially large aggregate is higher for those injected with BIS-crosslinked microgels than for those injected with ULC microgels. Since ULCs do not form these massive aggregates, they are not as high of a toxicity risk.

From a contrarian standpoint, aggregate formation may be a useful behavior. All microgel crosslinking conditions form aggregates that are at least temporarily trapped in lung and kidney microvasculature. This could be exploited by using microgels to specifically deliver therapeutic cargo to lungs or kidneys, without the need for additional targeting moieties. For example, antifibrotic medications such as nintedanib (brand name Ofev or Vargatef) could be loaded into microgels and injected into patients with idiopathic pulmonary fibrosis, limiting off-target effects. The challenge would be ensuring that aggregate size is stabilized, perhaps by copolymerizing hydrophilic monomers into the microgel particle.

4.6 Conclusion

The work presented here adds to our understanding of pNIPAM-based microgel pharmacokinetics, which is critical to advancing microgel technology to the clinical space. I find here that regardless of crosslinking density, most pNIPAM-AAc microgels are

cleared from blood within 12 hours, but accumulate in tissues such as lungs and kidneys. Furthermore, I demonstrate that crosslinked microgels more readily form large aggregates in blood that occlude lung microvasculature and have the potential to cause fatal toxic events. It is likely that aggregation is driven by hydrophobic forces; thus, this research underscores that microgels intended to be used *in vivo* should be composed of polymers that remain hydrophilic in physiologic conditions.

CHAPTER 5. OVERALL CONCLUSIONS AND FUTURE DIRECTIONS

Over the past two decades, there has been a massive surge in research involving microgels for biomedical applications. Because of their tunability, ease of synthesis, and ability to hold large amounts of therapeutic cargo relative to their size, microgels are an ideal platform for drug delivery, imaging, and biosensors. Yet despite promising preliminary data, only a couple of microgel-based therapies have reached clinical trials. A major obstacle for clinical translation of microgels is their rapid clearance and toxic or off-target effects *in vivo*, which motivated this work.

The work presented here demonstrated that crosslinking predictably increases the Young's, shear, and bulk moduli of pNIPAM-AAc microgels. Additionally, this research shows, for the first time, the effect of exposure to blood plasma on the mechanical properties of individual microgels. While plasma binding stiffens ULC and 8% BIS-crosslinked microgels, it has minimal effect on the stiffness of 2% BIS-crosslinked microgels, which was unexpected. Furthermore, these studies pioneered the use of multiple AFM nanoindentation techniques to tease out the shear and bulk moduli of pNIPAM-AAc microgels, revealing that bulk modulus is lower than shear modulus for all microgels studied, regardless of solvent. This indicates that it requires less force to compress microgels than to shear them, which may be useful in predicting their behavior in blood flow.

Beyond single-microgel mechanical analysis, this thesis also investigated how crosslinking affects the bulk behavior of microgels in whole blood. At common therapeutic doses, microgels do not affect the apparent viscosity of blood, suggesting that they do not induce significant hemolysis or affect RBC deformability and aggregation. One surprising result was that microgels do not readily marginate to the walls of microchannels, regardless of crosslinking density. Based on models of platelet margination and reports of leukocyte softening leading to demargination (*115, 121*), I had originally hypothesized that BIS-crosslinked microgels would marginate more effectively than ULC microgels. The finding that none of the microgels marginated effectively may be because even the stiffest are not sufficiently stiffer than RBCs. Those designing microgels for therapeutic delivery to vasculature may therefore aim to generate even stiffer microgels to enable margination and higher effective doses at the vessel wall.

An obvious extension of this work is to investigate the mechanical behaviors of other varieties of microgels, such as those formed from PEG. It has been shown that different polymers bind different proteins in plasma (*49*), so it stands to reason that their mechanical response to plasma exposure may differ as well. Furthermore, microgels synthesized with hollow cores, such as those developed by the Brown group (*5*) will likely have drastically different mechanical properties and swelling kinetics. The experiments and analyses outlined in this work can serve as a toolkit for interrogating the mechanics of any type of microgel particle.

Toward the goal of characterizing pNIPAM-AAc microgel behavior *in vivo*, I hypothesized that ULC microgels would exhibit a longer circulation time than BIS-crosslinked microgels, based on work by Merkel et al. that demonstrated longer half-lives

with hydrogels of lower modulus (*96*). However, my results indicated that regardless of crosslink density, pNIPAM-AAc microgels display a very short circulation time in blood, with a half-life on the order of a few hours, and are completely undetectable in blood after 30 hours. Interestingly, the microgels (and especially BIS-crosslinked microgels) seem to accumulate in lungs, and especially kidneys, for up to several days after injection. A key difference between these microgels and the hydrogels developed in the Merkel study is size: whereas all microgels in this study had a diameter of approximately 1 μm, hydrogels in the Merkel study were designed to mimic RBCs, which are considerably larger and discoid-shaped. To extend circulation time of pNIPAM-AAc microgles, a straightforward continuation of the work in this thesis could be to test so-called "giant" ULC (GULC) microgels developed by the Lyon group, which are about 8 μm in diameter (*23*).

A critical aspect to *in vivo* clearance of biomaterials is their likelihood of being internalized by components of the mononuclear phagocytic system (MPS). Previous work has shown that both the microgel polymer core and the components of its protein corona *in vivo* influence the degree of uptake by the MPS (*39, 40*). Furthermore, it has been shown that nanoparticle stiffness influences whether particles are internalized by micropinocytosis or clathrin-mediated endocytosis (*28*). Since the work presented here demonstrates that crosslink density clearly influences microgel stiffness *in vivo*, and that crosslinking may cause microgels to bind plasma proteins differently, future work on pNIPAM-AAc microgels should explore the effect of crosslinking on MPS uptake.

One of the most striking observations of this work was the effect of crosslinking density on microgel aggregation. Results presented here point to hydrophobic forces as a

primary driver of aggregation, though a critical question remains: Is aggregation caused by hydrophobic interactions between pNIPAM chains, or binding between corona proteins that differentially bind microgels through hydrophobic interactions? On one hand, the data in this thesis agrees with previous literature on the influence of plasma proteins on microgel aggregation. Miceli et al. found that hydrophobic collapse of pNIPAM-based microgels led to immunoglobulin binding, and subsequent aggregation (*49*), which agrees with data in **Figure 24.** This data also suggests that albumin may promote aggregation more potently than immunoglobulin. Thus, one could hypothesize that the corona of BIS-crosslinked microgels contains a greater proportion of albumin than that of ULC microgels. However, **Figure 25** demonstrates that if BIS-crosslinked microgels bind a greater proportion of albumin, the effect size is minimal. Beyond the biochemical composition of the protein corona, it may be also be useful to evaluate the morphology of microgels of varying crosslink density after corona formation using scanning electron microscopy.

However, based on the results in deionized water, it is apparent that protein corona alone cannot fully explain the crosslink-dependent aggregation behavior. It is possible that BIS-crosslinking confers enhanced hydrophobicity to pNIPAM-AAc microgels, leading to greater aggregation. Future studies of this behavior should include pNIPAM-AAc microgels that have been copolymerized with a stably hydrophilic monomer such as PEG to elucidate the effects of hydrophobicity on microgel aggregation *in vivo*.

Microgel aggregates were found to be large and durable enough to occlude lung microvasculature as modeled by a microfluidic device, though there are limitations to this experiment. For one, results in whole blood were complicated by upstream clotting in the device, leading to inconsistent flow and occasional large platelet aggregates that were not

associated with the microgel treatment. Additionally, the microchannels in the device recapitulating lung microvasculature were too small to be endothelialized with current protocols, which precluded assays of endothelial damage in a relevant model. Ongoing improvements in fabricating and endothelializing microfluidic devices for blood flow will allow for more accurate models of endothelial damage in the lung.

Surprisingly, the tendency of BIS-crosslinked microgels to form large aggregates in plasma did not lead to broadly enhanced inflammation in the mice that received them. There was some evidence of localized inflammation and tissue damage in lung sections, but this did not translate to reliably elevated cytokine expression or cell infiltration. I postulate here that the observed toxicity in certain mice may reflect a catastrophic event from especially large microgels, akin to a pulmonary embolism. While not every dose of microgels might result in such large aggregates, the risk is higher for BIS-crosslinked microgels. To explore this possibility further, a much larger animal study would be required in order to obtain sufficient statistical power.

Instead of viewing aggregation as something to be avoided, it is intriguing to imagine exploiting this behavior for therapeutic delivery. This work has shown that pNIPAM-AAc microgels of all types accumulate in the lungs and kidneys, apparently without causing large-scale inflammation. If the maximum aggregate size can be stabilized to a point where it no longer poses the threat of catastrophic occlusion, perhaps by copolymerizing especially hydrophilic polymers such as PEG, microgel aggregates could be an ideal vehicle for delivering molecules to lungs or kidneys, without the need for additional targeting moieties. This strategy is not without precedent; Deshmukh et al. showed that stabilized aggregates of PEG microgels accumulate in the lungs without toxic

side effects and can be utilized for delivery of therapeutic cargo (*106*). Since pNIPAM-AAc microgels spontaneously form aggregates in plasma, future development of a similar strategy would need to focus on optimizing aggregate size through crosslinking and co-polymer composition.

In summary, this thesis contributes to our knowledge about the mechanical responses of pNIPAM-AAc microgels, and how they respond to physiologic conditions. Furthermore, the methods outlined in this work give future researchers a reliable toolbox for interrogating the mechanical properties of a wide range of microgel constructs. Finally, this work demonstrates that crosslinking pNIPAM-AAc microgels with BIS leads to a greater propensity for aggregation, with potential toxic effects *in vivo*. While this thesis may be read as a cautionary tale for those designing similar microgel systems, I also present ideas for avoiding truly catastrophic aggregation-related events, and offer the potential for exploiting microgel aggregation to assist in passively targeted therapeutic delivery to lungs and kidneys.

REFERENCES

1. K. S. Soni, S. S. Desale, T. K. Bronich, Nanogels: An overview of properties, biomedical applications and obstacles to clinical translation. *J Control Release* **240**, 109-126 (2016).

2. G. R. Hendrickson, M. H. Smith, A. B. South, L. A. Lyon, Design of Multiresponsive Hydrogel Particles and Assemblies. *Adv Funct Mater* **20**, 1697-1712 (2010).

3. J. P. Rolland *et al.*, Direct fabrication and harvesting of monodisperse, shape-specific nanobiomaterials. *J Am Chem Soc* **127**, 10096-10100 (2005).

4. F. R. Kersey, T. J. Merkel, J. L. Perry, M. E. Napier, J. M. DeSimone, Effect of Aspect Ratio and Deformability on Nanoparticle Extravasation through Nanopores. *Langmuir* **28**, 8773-8781 (2012).

5. E. P. Sproul, S. Nandi, C. Roosa, L. Schreck, A. C. Brown, Biomimetic Microgels with Controllable Deformability Improve Healing Outcomes. *Adv Biosyst* **2**, (2018).

6. H. Senff, W. Richtering, Influence of cross-link density on rheological properties of temperature-sensitive microgel suspensions. *Colloid Polym Sci* **278**, 830-840 (2000).

7. M. S. Wolfe, Dispersion and Solution Rheology Control with Swellable Microgels. *Prog Org Coat* **20**, 487-500 (1992).

8. L. A. Lyon *et al.*, Microgel colloidal crystals. *J Phys Chem B* **108**, 19099-19108 (2004).

9. D. Suzuki, J. G. McGrath, H. Kawaguchi, L. A. Lyon, Colloidal crystals of thermosensitive, core/shell hybrid microgels. *J Phys Chem C* **111**, 5667-5672 (2007).

10. C. E. Reese, A. V. Mikhonin, M. Kamenjicki, A. Tikhonov, S. A. Asher, Nanogel nanosecond photonic crystal optical switching. *J Am Chem Soc* **126**, 1493-1496 (2004).

11. S. Q. Xu, J. G. Zhang, C. Paquet, Y. K. Lin, E. Kumacheva, From hybrid microgels to photonic crystals. *Adv Funct Mater* **13**, 468-472 (2003).

12. Z. Y. Meng, J. K. Cho, S. Debord, V. Breedveld, L. A. Lyon, Crystallization behavior of soft, attractive microgels. *J Phys Chem B* **111**, 6992-6997 (2007).

13. K. Ogawa, B. Wang, E. Kokufuta, Enzyme-regulated microgel collapse for controlled membrane permeability. *Langmuir* **17**, 4704-4707 (2001).

14. R. Pelton, Temperature-sensitive aqueous microgels. *Adv Colloid Interfac* **85**, 1-33 (2000).

15. X. J. Zhang, S. Malhotra, M. Molina, R. Haag, Micro- and nanogels with labile crosslinks - from synthesis to biomedical applications. *Chem Soc Rev* **44**, 1948-1973 (2015).

16. J. Gao, B. J. Frisken, Cross-linker-free N-isopropylacrylamide gel nanospheres. *Langmuir* **19**, 5212-5216 (2003).

17. Y. Sasaki, K. Akiyoshi, Nanogel Engineering for New Nanobiomaterials: From Chaperoning Engineering to Biomedical Applications. *Chem Rec* **10**, 366-376 (2010).

18. J. Gao, B. J. Frisken, Influence of reaction conditions on the synthesis of self-cross-linked N-isopropylacrylamide microgels. *Langmuir* **19**, 5217-5222 (2003).

19. Z. Y. Meng, M. H. Smith, L. A. Lyon, Temperature-programmed synthesis of micron-sized multi-responsive microgels. *Colloid Polym Sci* **287**, 277-285 (2009).

20. A. F. Routh, B. Vincent, Salt-induced homoaggregation of poly(N-isopropylacrylamide) microgels. *Langmuir* **18**, 5366-5369 (2002).

21. S. M. Hashmi, E. R. Dufresne, Mechanical properties of individual microgel particles through the deswelling transition. *Soft Matter* **5**, 3682-3688 (2009).

22. O. Tagit, N. Tomczak, G. J. Vancso, Probing the morphology and nanoscale mechanics of single poly(N-isopropylacrylamide) microgels across the lower-critical-solution temperature by atomic force microscopy. *Small* **4**, 119-126 (2008).

23. H. Bachman *et al.*, Ultrasoft, highly deformable microgels. *Soft Matter* **11**, 2018-2028 (2015).

24. S. Saxena *et al.*, Microgel film dynamics modulate cell adhesion behavior. *Soft Matter* **10**, 1356-1364 (2014).

25. D. E. Discher, P. Janmey, Y. L. Wang, Tissue cells feel and respond to the stiffness of their substrate. *Science* **310**, 1139-1143 (2005).

26. X. W. Huang *et al.*, Matrix Stiffness-Induced Myofibroblast Differentiation Is Mediated by Intrinsic Mechanotransduction. *Am J Resp Cell Mol* **47**, 340-348 (2012).

27. W. L. Murphy, T. C. McDevitt, A. J. Engler, Materials as stem cell regulators. *Nature Materials* **13**, 547-557 (2014).

28. X. Banquy *et al.*, Effect of mechanical properties of hydrogel nanoparticles on macrophage cell uptake. *Soft Matter* **5**, 3984-3991 (2009).

29. T. J. Merkel *et al.*, Using mechanobiological mimicry of red blood cells to extend circulation times of hydrogel microparticles. *P Natl Acad Sci USA* **108**, 586-591 (2011).

30. C. C. Fleischer, C. K. Payne, Nanoparticle-cell interactions: molecular structure of the protein corona and cellular outcomes. *Acc Chem Res* **47**, 2651-2659 (2014).

31. H. C. Fischer, T. S. Hauck, A. Gomez-Aristizabal, W. C. W. Chan, Exploring Primary Liver Macrophages for Studying Quantum Dot Interactions with Biological Systems. *Adv Mater* **22**, 2520-2524 (2010).

32. A. M. Derfus, W. C. W. Chan, S. N. Bhatia, Probing the cytotoxicity of semiconductor quantum dots. *Nano Lett* **4**, 11-18 (2004).

33. A. E. Nel *et al.*, Understanding biophysicochemical interactions at the nano-bio interface. *Nature Materials* **8**, 543-557 (2009).

34. Z. J. Deng, M. T. Liang, M. Monteiro, I. Toth, R. F. Minchin, Nanoparticle-induced unfolding of fibrinogen promotes Mac-1 receptor activation and inflammation. *Nat Nanotechnol* **6**, 39-44 (2011).

35. S. M. Moghimi *et al.*, Complement activation cascade triggered by PEG-PL engineered nanomedicines and carbon nanotubes: The challenges ahead. *Journal of Controlled Release* **146**, 175-181 (2010).

36. S. Zhang, J. Li, G. Lykotrafitis, G. Bao, S. Suresh, Size-Dependent Endocytosis of Nanoparticles. *Adv Mater* **21**, 419-424 (2009).

37. D. R. Absolom, Opsonins and dysopsonins: an overview. *Methods Enzymol* **132**, 281-318 (1986).

38. A. Vonarbourg, C. Passirani, P. Saulnier, J. P. Benoit, Parameters influencing the stealthiness of colloidal drug delivery systems. *Biomaterials* **27**, 4356-4373 (2006).

39. L. K. Muller *et al.*, Pre-coating with protein fractions inhibits nano-carrier aggregation in human blood plasma. *Rsc Adv* **6**, 96495-96509 (2016).

40. J. Simon *et al.*, Exploiting the biomolecular corona: pre-coating of nanoparticles enables controlled cellular interactions. *Nanoscale* **10**, 10731-10739 (2018).

41. C. D. Walkey, W. C. W. Chan, Understanding and controlling the interaction of nanomaterials with proteins in a physiological environment. *Chem Soc Rev* **41**, 2780-2799 (2012).

42. S. P. Boulos *et al.*, Nanoparticle-Protein Interactions: A Thermodynamic and Kinetic Study of the Adsorption of Bovine Serum Albumin to Gold Nanoparticle Surfaces. *Langmuir* **29**, 14984-14996 (2013).

43. R. Gref *et al.*, 'Stealth' corona-core nanoparticles surface modified by polyethylene glycol (PEG): influences of the corona (PEG chain length and surface density) and of the core composition on phagocytic uptake and plasma protein adsorption. *Colloids Surf B Biointerfaces* **18**, 301-313 (2000).

44. C. D. Walkey, J. B. Olsen, H. Guo, A. Emili, W. C. Chan, Nanoparticle size and surface chemistry determine serum protein adsorption and macrophage uptake. *J Am Chem Soc* **134**, 2139-2147 (2012).

45. A. Gessner, A. Lieske, B. R. Paulke, R. H. Muller, Functional groups on polystyrene model nanoparticles: Influence on protein adsorption. *J Biomed Mater Res A* **65a**, 319-326 (2003).

46. D. T. Jayaram, S. M. Pustulka, R. G. Mannino, W. A. Lam, C. K. Payne, Protein Corona in Response to Flow: Effect on Protein Concentration and Structure. *Biophys J* **115**, 209-216 (2018).

47. J. O'Brien, K. J. Shea, Tuning the Protein Corona of Hydrogel Nanoparticles: The Synthesis of Abiotic Protein and Peptide Affinity Reagents. *Accounts Chem Res* **49**, 1200-1210 (2016).

48. T. Cedervall *et al.*, Detailed identification of plasma proteins adsorbed on copolymer nanoparticles. *Angew Chem Int Edit* **46**, 5754-5756 (2007).

49. E. Miceli *et al.*, Understanding the elusive protein corona of thermoresponsive nanogels. *Nanomedicine (Lond)* **13**, 2657-2668 (2018).

50. A. C. Brown *et al.*, Ultrasoft microgels displaying emergent platelet-like behaviours. *Nat Mater* **13**, 1108-1114 (2014).

51. P. Kodlekere, L. Andrew Lyon, Microgel core/shell architectures as targeted agents for fibrinolysis. *Biomater Sci* **6**, 2054-2058 (2018).

52. E. Mihalko, K. Huang, E. Sproul, K. Cheng, A. C. Brown, Targeted Treatment of Ischemic and Fibrotic Complications of Myocardial Infarction Using a Dual-Delivery Microgel Therapeutic. *ACS Nano* **12**, 7826-7837 (2018).

53. A. V. Kabanov, S. V. Vinogradov, Nanogels as Pharmaceutical Carriers: Finite Networks of Infinite Capabilities. *Angew Chem Int Edit* **48**, 5418-5429 (2009).

54. V. P. Torchilin, Multifunctional nanocarriers. *Adv Drug Deliver Rev* **64**, 302-315 (2012).

55. T. K. Bronich, S. V. Vinogradov, A. V. Kabanov, Interaction of nanosized copolymer networks with oppositely charged amphiphilic molecules. *Nano Lett* **1**, 535-540 (2001).

56. S. V. Vinogradov, Colloidal microgels in drug delivery applications. *Curr Pharm Design* **12**, 4703-4712 (2006).

57. J. O. Kim, G. Sahay, A. V. Kabanov, T. K. Bronich, Polymeric Micelles with Ionic Cores Containing Biodegradable Cross-Links for Delivery of Chemotherapeutic Agents. *Biomacromolecules* **11**, 919-926 (2010).

58. Y. J. Wang, H. J. Xu, J. Wang, L. Ge, J. B. Zhu, Development of a Thermally Responsive Nanogel Based on Chitosan-Poly(N-Isopropylacrylamide-co-Acrylamide) for Paclitaxel Delivery. *J Pharm Sci-Us* **103**, 2012-2021 (2014).

59. S. Daoud-Mahammed *et al.*, Cyclodextrin and Polysaccharide-Based Nanogels: Entrapment of Two Hydrophobic Molecules, Benzophenone and Tamoxifen. *Biomacromolecules* **10**, 547-554 (2009).

60. S. Vinogradov, E. Batrakova, A. Kabanov, Poly(ethylene glycol)-polyethyleneimine NanoGel (TM) particles: novel drug delivery systems for antisense oligonucleotides. *Colloid Surface B* **16**, 291-304 (1999).

61. D. J. Siegwart *et al.*, Combinatorial synthesis of chemically diverse core-shell nanoparticles for intracellular delivery. *P Natl Acad Sci USA* **108**, 12996-13001 (2011).

62. J. Ramos, J. Forcada, R. Hidalgo-Alvarez, Cationic polymer nanoparticles and nanogels: from synthesis to biotechnological applications. *Chem Rev* **114**, 367-428 (2014).

63. U. Hasegawa *et al.*, Raspberry-like assembly of cross-linked nanogels for protein delivery. *Journal of Controlled Release* **140**, 312-317 (2009).

64. K. Nagahama, T. Ouchi, Y. Ohya, Biodegradable Nanogels Prepared by Self-Assembly of Poly(L-lactide)-Grafted Dextran: Entrapment and Release of Proteins. *Macromol Biosci* **8**, 1044-1052 (2008).

65. L. J. Shi, S. Khondee, T. H. Linz, C. Berkland, Poly(N-vinylformamide) nanogels capable of pH-sensitive protein release. *Macromolecules* **41**, 6546-6554 (2008).

66. W. Chen *et al.*, In Situ Forming Reduction-Sensitive Degradable Nanogels for Facile Loading and Triggered Intracellular Release of Proteins. *Biomacromolecules* **14**, 1214-1222 (2013).

67. T. Nochi *et al.*, Nanogel antigenic protein-delivery system for adjuvant-free intranasal vaccines. *Nature Materials* **9**, 572-578 (2010).

68. S. Kitano *et al.*, HER2-specificT-cell immune responses in patients vaccinated with truncated HER2 protein complexed with nanogels of cholesteryl pullulan. *Clin Cancer Res* **12**, 7397-7405 (2006).

69. A. Uenaka *et al.*, T cell immunomonitoring and tumor responses in patients immunized with a complex of cholesterol-bearing hydrophobized pullulan (CHP) and NY-ESO-1 protein. *Cancer Immun* **7**, 9 (2007).

70. S. Kageyama *et al.*, Dose-dependent effects of NY-ESO-1 protein vaccine complexed with cholesteryl pullulan (CHP-NY-ESO-1) on immune responses and survival benefits of esophageal cancer patients. *J Transl Med* **11**, 246 (2013).

71. K. Katagiri *et al.*, Templated nucleation of hybrid iron oxide nanoparticles on polysaccharide nanogels. *Colloid Polym Sci* **291**, 1375-1380 (2013).

72. E. S. G. Choo, X. S. Tang, Y. Sheng, B. Shuter, J. M. Xue, Controlled loading of superparamagnetic nanoparticles in fluorescent nanogels as effective T-2-weighted MRI contrast agents. *J Mater Chem* **21**, 2310-2319 (2011).

73. A. Soleimani *et al.*, Polymer cross-linking: a nanogel approach to enhancing the relaxivity of MRI contrast agents. *J Mater Chem B* **1**, 1027-1034 (2013).

74. C. Paquet *et al.*, Clusters of Superparamagnetic Iron Oxide Nanoparticles Encapsulated in a Hydrogel: A Particle Architecture Generating a Synergistic Enhancement of the T-2 Relaxation. *Acs Nano* **5**, 3104-3112 (2011).

75. S. Okada, S. Mizukami, Y. Matsumura, Y. Yoshioka, K. Kikuchi, A nanospherical polymer as an MRI sensor without paramagnetic or superparamagnetic species. *Dalton T* **42**, 15864-15867 (2013).

76. C. K. Lim *et al.*, Gadolinium-coordinated elastic nanogels for in vivo tumor targeting and imaging. *Biomaterials* **34**, 6846-6852 (2013).

77. N. Lewinski, V. Colvin, R. Drezek, Cytotoxicity of nanoparticles. *Small* **4**, 26-49 (2008).

78. J. Kim, Y. Piao, T. Hyeon, Multifunctional nanostructured materials for multimodal imaging, and simultaneous imaging and therapy. *Chem Soc Rev* **38**, 372-390 (2009).

79. J. Lux, A. G. White, M. Chan, C. J. Anderson, A. Almutairi, Nanogels from metal-chelating crosslinkers as versatile platforms applied to copper-64 PET imaging of tumors and metastases. *Theranostics* **5**, 277-288 (2015).

80. S. Singh *et al.*, Radiolabeled Nanogels for Nuclear Molecular Imaging. *Macromol Rapid Comm* **34**, 562-567 (2013).

81. J. Yu *et al.*, Self-Assembly Synthesis, Tumor Cell Targeting, and Photothermal Capabilities of Antibody-Coated Indocyanine Green Nanocapsules. *J Am Chem Soc* **132**, 1929-1938 (2010).

82. H. S. Park *et al.*, Hyaluronic Acid/Poly(ss-Amino Ester) Polymer Nanogels for Cancer-Cell-Specific NIR Fluorescence Switch. *Macromol Rapid Comm* **33**, 1549-1555 (2012).

83. J. Kim, Y. Chong, H. Mok, Shell-crosslinked hyaluronic acid nanogels for live monitoring of hyaluronidase activity in vivo. *Macromol Biosci* **14**, 881-888 (2014).

84. Y. W. Noh *et al.*, Near-infrared emitting polymer nanogels for efficient sentinel lymph node mapping. *ACS Nano* **6**, 7820-7831 (2012).

85. L. V. Sigolaeva *et al.*, Engineering Systems with Spatially Separated Enzymes via Dual-Stimuli-Sensitive Properties of Microgels. *Langmuir* **31**, 13029-13039 (2015).

86. L. V. Sigolaeva *et al.*, Surface Functionalization by Stimuli-Sensitive Microgels for Effective Enzyme Uptake and Rational Design of Biosensor Setups. *Polymers-Basel* **10**, (2018).

87. L. V. Sigolaeva *et al.*, Dual-Stimuli-Sensitive Microgels as a Tool for Stimulated Spongelike Adsorption of Biomaterials for Biosensor Applications. *Biomacromolecules* **15**, 3735-3745 (2014).

88. L. V. Sigolaeva *et al.*, A layer-by-layer tyrosinase biosensor for assay of carboxylesterase and neuropathy target esterase activities in blood. *Anal Methods-Uk* **5**, 3872-3879 (2013).

89. L. V. Sigolaeva *et al.*, Easy-Preparable Butyrylcholinesterase/Microgel Construct for Facilitated Organophosphate Biosensing. *Anal Chem* **89**, 6092-6099 (2017).

90. S. V. Vinogradov, Nanogels in the race for drug delivery. *Nanomedicine (Lond)* **5**, 165-168 (2010).

91. Y. Li, K. Xiao, W. Zhu, W. Deng, K. S. Lam, Stimuli-responsive cross-linked micelles for on-demand drug delivery against cancers. *Adv Drug Deliv Rev* **66**, 58-73 (2014).

92. S. M. Moghimi, C. J. Porter, I. S. Muir, L. Illum, S. S. Davis, Non-phagocytic uptake of intravenously injected microspheres in rat spleen: influence of particle size and hydrophilic coating. *Biochem Biophys Res Commun* **177**, 861-866 (1991).

93. L. Zhang *et al.*, Softer zwitterionic nanogels for longer circulation and lower splenic accumulation. *ACS Nano* **6**, 6681-6686 (2012).

94. M. Elsabahy, K. L. Wooley, Design of polymeric nanoparticles for biomedical delivery applications. *Chem Soc Rev* **41**, 2545-2561 (2012).

95. Y. Geng *et al.*, Shape effects of filaments versus spherical particles in flow and drug delivery. *Nat Nanotechnol* **2**, 249-255 (2007).

96. T. J. Merkel *et al.*, Using mechanobiological mimicry of red blood cells to extend circulation times of hydrogel microparticles. *Proc Natl Acad Sci U S A* **108**, 586-591 (2011).

97. K. Shiraishi *et al.*, Hydrophobic blocks of PEG-conjugates play a significant role in the accelerated blood clearance (ABC) phenomenon. *J Control Release* **165**, 183-190 (2013).

98. T. Ishihara *et al.*, Accelerated blood clearance phenomenon upon repeated injection of PEG-modified PLA-nanoparticles. *Pharm Res* **26**, 2270-2279 (2009).

99. T. Ishida *et al.*, Accelerated blood clearance of PEGylated liposomes following preceding liposome injection: effects of lipid dose and PEG surface-density and chain length of the first-dose liposomes. *J Control Release* **105**, 305-317 (2005).

100. R. B. Campbell *et al.*, Cationic charge determines the distribution of liposomes between the vascular and extravascular compartments of tumors. *Cancer Res* **62**, 6831-6836 (2002).

101. M. Nakamura, P. Davila-Zavala, H. Tokuda, Y. Takakura, M. Hashida, Uptake and gene expression of naked plasmid DNA in cultured brain microvessel endothelial cells. *Biochem Biophys Res Commun* **245**, 235-239 (1998).

102. H. Lv, S. Zhang, B. Wang, S. Cui, J. Yan, Toxicity of cationic lipids and cationic polymers in gene delivery. *J Control Release* **114**, 100-109 (2006).

103. B. Naeye *et al.*, Hemocompatibility of siRNA loaded dextran nanogels. *Biomaterials* **32**, 9120-9127 (2011).

104. P. R. Sarika, P. R. Anil Kumar, D. K. Raj, N. R. James, Nanogels based on alginic aldehyde and gelatin by inverse miniemulsion technique: synthesis and characterization. *Carbohydr Polym* **119**, 118-125 (2015).

105. A. G. Koutsiaris, S. V. Tachmitzi, N. Batis, Wall shear stress quantification in the human conjunctival pre-capillary arterioles in vivo. *Microvasc Res* **85**, 34-39 (2013).

106. M. Deshmukh *et al.*, Biodistribution and renal clearance of biocompatible lung targeted poly(ethylene glycol) (PEG) nanogel aggregates. *J Control Release* **164**, 65-73 (2012).

107. Y. Wang, R. Zhao, R. G. Russell, I. D. Goldman, Localization of the murine reduced folate carrier as assessed by immunohistochemical analysis. *Biochim Biophys Acta* **1513**, 49-54 (2001).

108. S. K. Desmoulin, Z. Hou, A. Gangjee, L. H. Matherly, The human proton-coupled folate transporter: Biology and therapeutic applications to cancer. *Cancer Biol Ther* **13**, 1355-1373 (2012).

109. S. Frokjaer, D. E. Otzen, Protein drug stability: a formulation challenge. *Nat Rev Drug Discov* **4**, 298-306 (2005).

110. R. Krishnamurthy, M. C. Manning, The stability factor: importance in formulation development. *Curr Pharm Biotechnol* **3**, 361-371 (2002).

111. T. J. Kamerzell, R. Esfandiary, S. B. Joshi, C. R. Middaugh, D. B. Volkin, Protein-excipient interactions: mechanisms and biophysical characterization applied to protein formulation development. *Adv Drug Deliv Rev* **63**, 1118-1159 (2011).

112. T. M. Allen, Ligand-targeted therapeutics in anticancer therapy. *Nat Rev Cancer* **2**, 750-763 (2002).

113. A. J. Gale, Continuing education course #2: current understanding of hemostasis. *Toxicol Pathol* **39**, 273-280 (2011).

114. O. K. Baskurt, H. J. Meiselman, Blood rheology and hemodynamics. *Semin Thromb Hemost* **29**, 435-450 (2003).

115. H. Zhao, E. S. G. Shaqfeh, V. Narsimhan, Shear-induced particle migration and margination in a cellular suspension. *Phys Fluids* **24**, (2012).

116. J. H. Haga, A. J. Beaudoin, J. G. White, J. Strony, Quantification of the passive mechanical properties of the resting platelet. *Ann Biomed Eng* **26**, 268-277 (1998).

117. S. Fitzgibbon, J. Cowman, A. J. Ricco, D. Kenny, E. S. G. Shaqfeh, Examining platelet adhesion via Stokes flow simulations and microfluidic experiments. *Soft Matter* **11**, 355-367 (2015).

118. C. D. Jones, L. A. Lyon, Synthesis and characterization of multiresponsive core-shell microgels. *Macromolecules* **33**, 8301-8306 (2000).

119. D. C. Lin, D. I. Shreiber, E. K. Dimitriadis, F. Horkay, Spherical indentation of soft matter beyond the Hertzian regime: numerical and experimental validation of hyperelastic models. *Biomech Model Mechan* **8**, 345-358 (2009).

120. B. Sierra-Martin *et al.*, Determination of the bulk modulus of microgel particles. *Colloid Polym Sci* **289**, 721-728 (2011).

121. M. E. Fay *et al.*, Cellular softening mediates leukocyte demargination and trafficking, thereby increasing clinical blood counts. *P Natl Acad Sci USA* **113**, 1987-1992 (2016).

122. M. J. Kim, S. Shin, Toxic effects of silver nanoparticles and nanowires on erythrocyte rheology. *Food Chem Toxicol* **67**, 80-86 (2014).

123. W. C. Wu *et al.*, Preoperative hematocrit levels and postoperative outcomes in older patients undergoing noncardiac surgery. *JAMA* **297**, 2481-2488 (2007).

124. R. A. Chachanidze, O; Wagner, C; Leonetti, M, in *8th World Congress of Biomechanics*. (Dublin, Ireland, 2018).

125. A. C. Anselmo *et al.*, Platelet-like nanoparticles: mimicking shape, flexibility, and surface biology of platelets to target vascular injuries. *ACS Nano* **8**, 11243-11253 (2014).

126. M. J. Rosenbluth, W. A. Lam, D. A. Fletcher, Analyzing cell mechanics in hematologic diseases with microfluidic biophysical flow cytometry. *Lab Chip* **8**, 1062-1070 (2008).

127. D. R. Myers *et al.*, Endothelialized Microfluidics for Studying Microvascular Interactions in Hematologic Diseases. *Jove-J Vis Exp*, (2012).

128. M. I. Townsley, Structure and composition of pulmonary arteries, capillaries, and veins. *Compr Physiol* **2**, 675-709 (2012).